Methods for performance characterization of artificial molecular motors

Unksov, Ivan

2021

Document Version:
Publisher's PDF, also known as Version of record

Division of Solid State Physics

Department of Physics

Lund University

Licentiate thesis

Methods for Performance Characterization of Artificial Molecular Motors

Author: Ivan N. Unksov

Main Supervisor: Prof. Heiner Linke

Co-supervisor: Prof. Sara Linse

LUND UNIVERSITY

Lund

2021

Preface

"Methods for performance characterization of artificial molecular motors" is a licentiate thesis by Ivan Unksov. With permission from coauthors, this thesis is in part based on the following manuscript:

Fluorescence excitation enhancement by waveguiding nanowires

Ivan Unksov, Nicklas Anttu, Damiano Verardo, Fredrik Höök, Christelle Prinz, Heiner Linke

Planned to be submitted to Nano Letters.

I made the samples, carried out the experimental part, analyzed the experimental data, made all figures that contain those data and wrote the parts of the article where the experimental data are discussed, with input from coauthors.

Public examination of this thesis is done by Assoc. Prof. Adam Burke on Thursday, the 29th of April 2021, at 15.00 online via zoom meeting ID: 621 9904 4328, password: 069710. Opponent of the thesis is Prof. Bo Wegge Laursen from Copenhagen University.

Abstract

The overall aim of this thesis work is to characterize artificial biomolecular motors, specifically the Lawnmower, a motor based on the burn bridges mechanism, and the Tumbleweed, a protein motor that employs ligand specific DNA-proteins binding to step along DNA. An overview of their operational principles is given, and initial results of our studies are presented, along with a review of currently available methods to characterize artificial molecular motors.

One way to characterize the expected 10-15 nm sized steps of Tumbleweed may be to harness the properties of waveguiding nanowires. An outline of such an approach is presented, and a detailed study of underlying physical phenomena is performed. Specifically, to understand what dimensions of nanowires should be used, we study the enhancement of fluorescence excitation, one of the phenomena contributing to guidance of light in gallium phosphide nanowires. We find experimentally, and confirm with modelling, that the nanowires with diameter around 110 nm and 10 nm thick Al_2O_3 coating maximize the enhancement for red fluorophores, and our modelling suggests that the optimum diameter shifts to smaller diameters for fluorophores with a shorter excitation wavelength. The nanowires are promising for many applications including biosensing.

Plans for further studies are also presented. Specifically, molecular motor studies are proposed on the Tumbleweed or similar motors. As for the nanowire studies, these may be continued using fluorescence-lifetime imaging microscopy (FLIM) which would show how the nanowires affect fluorescence emission, and towards the goal to use nanowires in biosensing which might also involve fluorescent noble metal nanoclusters.

Table of contents

Introduction

Molecular motors are constructs that propel themselves by harnessing thermal motion and molecular interactions. A variety of synthetic motors and designs have been created[1–13], with various applications in mind, including cargo transportation[11], switches and rotors[5,14–16], photoswitchable systems to record digital information[17], few atom sized machines employing quantum tunneling for directional motion[18], motors for photothermal therapy of cancer[19], formation of supramolecular assemblies capable of motion[13], manipulations with cells[10] etc. Synthetic molecular machines were acknowledged with a Nobel prize in Chemistry in 2016.

Two major classes of molecular machines are molecular walkers and rotary motors. Most of the above mentioned artificial motors are based on either DNA or non-biological molecules, unlike protein-based natural motors. Hence it is promising to use proteins to build artificial motors, as that would enable employing a vast variety of protein molecular interactions. One example of a protein based motor is the Lawnmower (LM) (Figure 1a) that we study and that is a fully autonomous molecular walker, which means that its motion is independent on any externally introduced agents. LM is a microbead or quantum dot decorated with proteases which irreversibly cleave peptide-containing 'lawn' on a surface when moving.

Another type of directional bias enables the motion of the second protein motor we study, the Tumbleweed (TW) (Figure 1b), a construct synthetized *de novo* from DNA-binding protein domains[20]. TW is designed to walk along a DNA track[21]. The directionality of the TW motion relies on a sequence of binding sites in the track and externally controlled changes of ligands in the buffer, such that it is in principle possible to change the motor's direction.

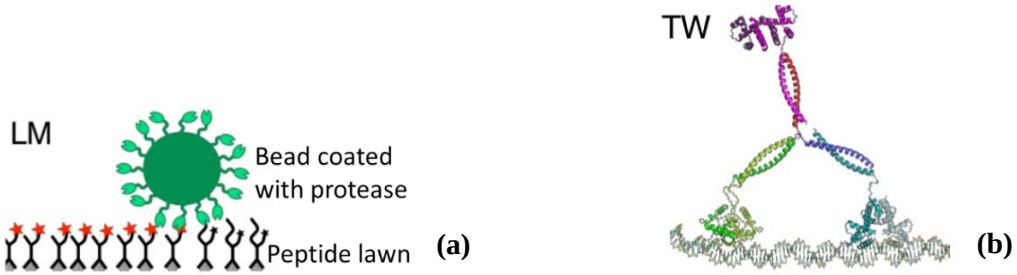

Figure 1. Molecular motors in this study: (a) Lawnmower moving due to cleavage of a peptide substate with its multiple protease legs; (b) Tumbleweed on a DNA track. *Reproduced under Open Access license from ref.* [20].

To prove that a synthetic molecular motor is functional, one needs to choose a suitable experimental technique to see its motion, either on single-molecule basis or in bulk experiments, for example using Förster resonance energy transfer (FRET). Some commonly used techniques are reviewed in this thesis.

Using displacements analysis for images from an optical microscope, we have characterized the motion of LMs made of 2.8 μm beads, and an overview of these experiments will also be presented.

Compared to LM, TW demands a more technically advanced method, because its steps along DNA are expected to be just 10-15 nm. As one possibility to characterize the stepping of TW, we are considering the use of waveguiding semiconductor nanowires (NWs), which have recently emerged for use in single-molecule detection[22] and, in general, biosensing[23–25] based on the guidance and enhancement of fluorescence.

Biosensing is an extensively studied field, because detection of small amounts of biomarkers, biological macromolecules, cells or viruses is important for healthcare and life sciences. An ideal biosensor is typically thought of as a 'black box' (e.g. a microfluidic device) in which a sample is placed, ideally without prior purification or concentrating, and the sensor indicates presence of a substance of interest. Thus, simplicity of detection and uniformity of multiple sensors are the characteristics sought after. A variety of nanostructure biosensors are employing plasmonics and waveguiding. Plasmons are oscillations of electrons occurring on surface of metal nanostructures. Surface plasmon resonance can be used for DNA and protein biosensors.[26,27] Plasmonic techniques are label-free, however fluorescence is also promising to employ in biosensing because it allows for detecting concentrations of molecules as little as single-molecule.

In the research article manuscript included in this thesis, a diameter 90-140 nm of gallium phosphide (GaP) nanowires (NWs) coated with Al_2O_3 is found to maximize the excitation enhancement of fluorescence of red fluorophores attached to the NWs. The excitation enhancement, together with guidance of light towards the tip of a NW and the modified radiative yield of a fluorophore, contributes to fluorescence enhancement and increased probability to detect emitted photons. We study the excitation enhancement using fluorescence microscopy, and the experimental result is supported with modelling. Our article provides a design guide for NW biosensors detecting fluorescence via lightguiding.

The motivation to use NWs observed with a microscope is due to the fact that, although growing nanowires is a rather difficult and expensive process e.g. done via metalorganic vapour-phase epitaxy (MOVPE), only a millimeter sized chip of a substrate with NWs is needed for a single device, and it is possible to achieve uniform dimensions of NWs and to scale-up their production. Development of nanofabrication technologies, e.g. displacement Talbot lithography[19] for nanopatterning, improves scalability and uniformity even further. As for simplicity of detection, in case of lightguiding, detection is done using a widefield microscope available in most research institutions, even though a weak signal in case of low concentration of fluorophores presents as issue which has to be circumvented by using a powerful source of light (laser) and employing denoising image analysis.

Additionally, this thesis involves a brief outlook on noble metal fluorescent nanoclusters templated by DNA, which is another growing field of nanobioscience, and is proposed as possible direction for our future research on molecular motors and lightguiding NWs.

Chapter 1. Principles of TW and LM motion and requirements for studying the motors

1.1. Lawnmower

The motion of molecular walkers typically involves a track, motion along which is typically desired to be processive and directional. This can be achieved by introducing directional bias in the track or motor, often by a burnt-bridges ratchet mechanism[1]. Burnt-bridges ratchet (BBR) motors rely on a mechanism by which the motor modifies a substrate such that it becomes non-binding or energetically unfavorable to bind to in the locations already passed by the motor. Because of that, the motor tends towards previously unexplored locations by diffusion, in addition to which some motors are themselves a source of forces, e.g. chemophoretic[28], that are not applied externally but result from the motor interactions with its substrate. This results in a superdiffusive motion, achieving which is the goal.

There is a range of superdiffusive BBR motors, including bead based motors created recently and showing processive motion[2,28,29] and molecular spiders [30–32] but, in contrast with LM, which is autonomous by its design, many of them move due to agents externally supplied to the buffer. Additionally, LM is a protein-based motor.

The diffusivity of the motion can be extracted from mean squared displacement (MSD) of multiple motors (ensemble-averaged MSD), or a single motor over time (time-averaged MSD)[33]: MSD $\propto D_g \tau^{\alpha}$ where D_g –

generalized diffusion constant, τ – time (for ensemble-averaged MSD) or time lag (for time-averaged MSD), α – anomalous diffusion coefficient. The motion is called superdiffusive when $\alpha > 1$.[7]

LM has multiple legs (motors of this type are known as polyvalent) attached to a 2.8 μm bead, and each leg incorporates a trypsin protease that cleaves the peptides on a substrate (Figure 1a). The cleavage rectifies diffusion of the motor, creating a directional bias towards previously unvisited substrate (Figure 2). The LM motion on 2D substrate has been recently studied in simulations[34] and experiments by our collaborators in Nancy Forde group at Simon Fraser University, who specialize in physics of artificial motors. Furthermore, it was found through Monte Carlo simulations that constraining the width of a substrate and thus arranging a quazi-1D track can facilitate superdiffusive motion of a polyvalent BBR motor, which on such a track also stays attached for a longer time compared to a 2D substrate.[35] Inspired by this result, we made peptide containing channels on SiO_2 to investigate the LM motion in the channels experimentally. We also studied the LM motion on peptide functionalized 2D SiO_2 surfaces. Our initial results are summarized in Section 3.1. of this thesis.

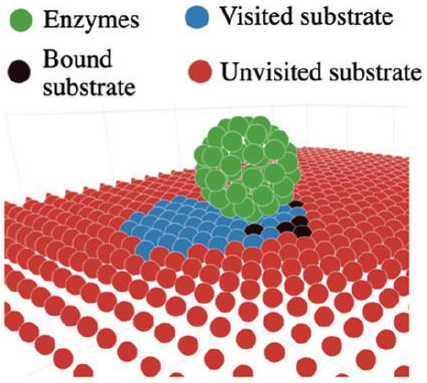

Figure 2. LM motor on a peptide substrate. *Reproduced from ref.[34] with permission from the Royal Society of Chemistry.*

1.2. Tumbleweed

TW is being designed and synthetized in Paul Curmi group at UNSW and has three protein domains (feet, see Figure 1b) which are repressors binding to a double stranded DNA oligonucleotide track; we use synthetic tracks with three repeated repressor-binding sequences. The binding each repressor depends on one of three ligands: S-Adenosyl methionine, L-tryptophane and $NiCl_2$. Thus, it is possible to switch pairs of ligands in buffer so that the TW feet sequentially bind and unbind, stepping onto the track in pairs to prevent the detachment of the entire motor from the track (Figure 3). TW bears a fluorescent label, however observation of its stepping is challenging for a number of reasons. Firstly, the steps covered by the motor are as small as 10-15 nm. Furthermore, DNA track has to be straight to ensure observation of the steps. The contour length of a minimal track, with only three binding sites (ABC), is about 40 nm which is close to the persistence length of the double stranded DNA (around 50 nm)[36]; therefore, the track can be slightly curved. Switching between buffers with different ligands needs to be done multiple times without perturbations in the DNA track; for that, a microfluidic device has been developed in our group[37]. Finally, in case of a repetitive ABC track, multiple identical motors can bind to identical sites in close proximity. Our current goal is to find a method to detect multiple steps of the TW, ideally controlling the direction.

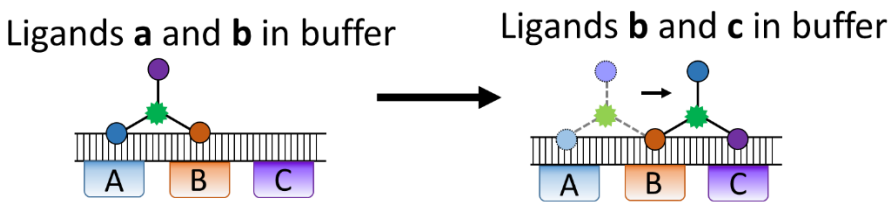

Figure 3. Tumbleweed steps along a DNA that has three binding sites (ABC), upon a change of ligands in the buffer. The motor consist of three protein domains, fluorescent label is in the centre of the construct. When the pair of ligands **a** and **b** is in the buffer, the TW is bound to sites A and B with two of the domains (blue and orange), and when the ligand pair is changed to **b** and **c**, the blue domain unbinds from A, and TW remains bound to B but also binds to C with the purple domain.

Chapter 2. Methods for characterization of artificial molecular motors

2.1. FRET and spectroscopy methods

Here we would like to introduce the techniques that have previously been used in molecular motor studies and are therefore options for our studies of the TW motor. The most extensively used methods for observing artificial molecular motors motion are microscopy, FRET and spectroscopy. In the following we review how these methods have been used previously to characterize synthetic molecular motors and evaluate them for possible use to study TW.

The efficiency of FRET is inversely proportional to $1 + \left(\frac{r}{R}\right)^6$, where r – the distance in a FRET pair, R – 50 % efficiency distance[38]. That stems from a spectral overlap between donor and acceptor; a larger overlap increases the distance[39] but also the parasitic signal. Parts of a moving motor are continuously repositioning relative to each other and to the track, and hence it is often possible to see the motion using FRET. For a DNA walker that moves due to hydrolysis of single stranded DNA serving as a fuel, the kinetics have been investigated by attachment of a FRET pair on the motor and fuel and observing FRET in the bulk[40,41], or, also in the bulk, mounting a fluorophore-quencher pair on motor and track and tracking the quenching[42]. For the TW motor, FRET would enable to see a single step of 10-15 nm if the motor and track are labelled with a FRET pair dyes. The position of a track attached dye would need to be fixed relative to the motor to reduce inaccuracy, which is a task in itself as the track DNA can wobble and curve.

Another popular tool for artificial molecular motors studies are spectroscopy techniques. For example, the Leigh group used ^{1}H NMR spectra to observe catenane rotary motor and a walker motor.[43,44] ^{1}H NMR, ^{13}C NMR and circular dichroism (CD) spectra were employed to distinguish between rotational states of a molecular rotor[5]. ^{1}H NMR and CD were used to observe photoinduced transitions of the motor[17]. However, spectroscopy typically requires fixed buffer conditions not feasible for TW, the motility of which relies on buffer change.

2.2. Microscopy techniques

Optical microscopy is diffraction limited because the Airy disk radius is the smallest distance over which several objects do not merge in a single spot. The $r = \frac{0.61\lambda}{\mathrm{NA}}$, where λ is the observed wavelength, NA is the numerical aperture of the objective. Consequently, optical microscopy is useful when the resolution beyond the diffraction limit is not required, e.g. for sufficiently large molecular motors like the bead-based LM, or when the motion is analyzed on a large scale. For example, fluorescent microscopy has been used, augmented by single molecule localization software and pre-processing smoothing and drift correction, for imaging and batch analysis of trajectories of DNA origami motors, even though each motor was smaller than a diffraction limited spot[28].

Total internal reflection fluorescence microscopy (TIRF) is still limited by diffraction but improves signal-to noise ratio. TIRF is often used for single molecule FRET or imaging of molecular motors. Noise is suppressed by harnessing the evanescent field of internally reflected light to avoid exciting fluorophores located deeper in the sample than the evanescent field penetrates, and thus to suppress the background signal. Intensity of the evanescent field decreases exponentially[38]. In prism-based TIRF, a prism enables the light to hit the coverslip, while the objective detects the fluorescence on the other side of the sample chamber. In more commonly used objective-based TIRF, both excitation and emission light goes through the objective in an inverted microscope[45]. Prism-based TIRF was used to detect a single molecule FRET signal of an operating, rotary DNA motor (Figure 4a, 4b)[46], while objective-based TIRF was used in another single molecule FRET observation of the motion of a DNA walker[47].

Objective-based TIRF requires an objective with a high numerical aperture (NA) because $\theta_c < \theta < \alpha$, where θ_c is the critical angle of total internal reflection, θ is the angle feasible for the objective, and $\alpha = \arcsin\left(\frac{\mathrm{NA}}{n}\right)$ for an immersion media with refractive index n. Therefore, larger NA enables larger TIRF angles which, in turn, allow for a less penetrative evanescent field. Oil immersion objectives have NA > 1.45, while $n_{\mathrm{oil}} \approx 1.51 \approx n_{\mathrm{glass}}$ minimizes reflections on the oil-glass interface.

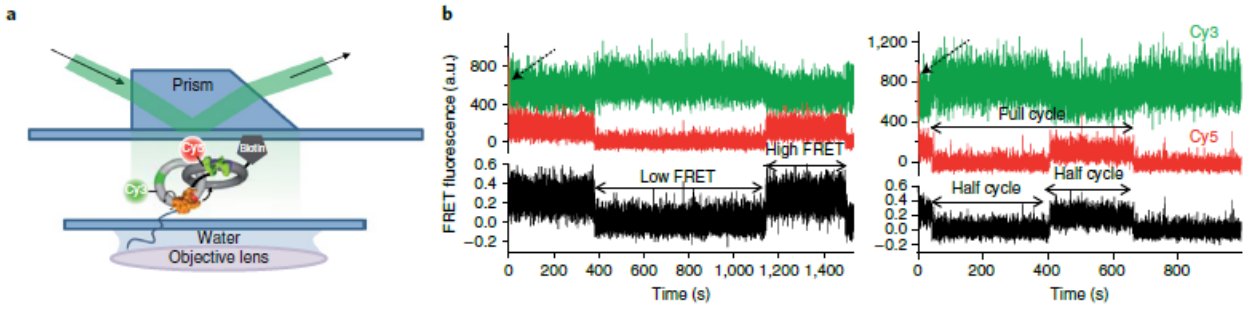

Figure 4. (a) Prism based TIRF and DNA catenane motor with attached FRET pair; (b) oscillating FRET signal upon rotation of the rotor ring of the motor. *Reproduced with permission from ref.* [46]. *Copyright © 2018, Springer Nature.*

Transmission electron microscopy (TEM) is also used to study motions of artificial motors, given that they are visible by electron microscopy after sample preparation. In recent studies, TEM was used to detect light-driven rotation, and formation of supramolecular assembles containing rotary motors, in combination with UV-Vis, CD and ^{1}H NMR spectroscopy and DLS.[13] TEM was also used to detect a Au nanorod motor moving along DNA origami positions.[48]

Atomic force microscopy (AFM) is a probe scanning technique which allows for nanometer resolution and can thus be used to see even small motors. AFM typically involves a laser and a probe which reflects the laser beam that then hits a segmented photodetector; therefore, position of the beam on the detector indicates the interaction between the probe and sample surface. High speed AFM (HS AFM) at frame rate 0.1 s^{-1} was used to observe steps of a DNA motor on a complementary track as small as 7.4 nm, the result was confirmed using fluorescence quenching of four fluorophores along the track by a quencher on the motor[49]. Through reducing dimensions of scanning by choosing a single line, HS AFM achieved the rate as high as 0.5-1 ms per line to observe dynamics of annexin-V trimers rotation[50].

Methods which by design surpass the diffraction limit are called superresolution techniques. These include stochastic optical reconstruction microscopy (STORM), photo-activation localization microscopy (PALM), stimulated emission depletion (STED) microscopy and structured illumination microcopy (SIM) which can be combined with TIRF. Superresolution techniques have been used to study a number of dynamic systems of natural molecular motors. For example, 50 nm spatial resolution and high temporal resolution was achieved using STED for proteins moving along a DNA stretched with optical tweezers[51], and up to 120

nm resolution was obtained for cytoskeletal protein moving filaments using TIRF-SIM[52]. To our knowledge, these techniques have not been applied to artificial molecular motors. As for the TW, superresolution methods could potentially resolve its motion over a several steps distance, but unlikely a single step.

Chapter 3. Characterization of Lawnmower and Tumbleweed.

3.1. Lawnmower

We studied the motion of LMs on SiO_2 coated with a brush of F127 polymers to which the peptides were attached, similar as in [53]. Time-averaged mean squared displacements were calculated for each motor as TA MSD $= \frac{1}{T-\tau}\sum_{t=0}^{T-\tau}(r(t+\tau)-r(t))^2$ where T – total measurement time, τ – time lag. For TA MSDs, the important parameter to choose is the maximum time lag τ over which the displacement is calculated, as calculating MSD over larger time lags may induce averaging out the actual MSDs trend[54]. We assumed 0.1 of the total duration of motion in a trajectory as the maximum time lag τ for that trajectory. From TA MSD for each motor, we calculated its anomalous diffusion coefficient (Section 1.1) as $\alpha = \frac{d(\log \mathrm{MSD})}{d(\log \tau)}$.

On a cleavable 2D peptide lawn, we observed (Figure 5a) a fraction of motors getting stuck due to nonspecific binding, while the others had α close to 1, thus not demonstrating any noticeable superdiffusion. The motion of those LMs was similar to that of LMs on no-peptide substrate (just F127 polymers) (Figure 5b). However, an intriguing observation was that when the protease activity was inhibited enzymatically, no LMs were moving (data not shown because α for all motors was about zero), which indicates that unspecific binding between LMs and the substrate may issue the motion, being outplayed (but not completely) by protease cleavage of the lawn.

Our major aim was to study the motion of LMs in quasi-1D channels (Figure 6a), constraining the motors in which was predicted by modelling to facilitate superdiffusion[35] and control the motion by guiding the motors along the channels serving as tracks. Using electron beam lithography, we fabricated 1.5, 2.2 and 2.8 μm wide channels in resist-coated SiO_2, the depth of which was adjusted so that the 2.8 μm sized LMs could touch the bottom of the channels; fabrication was done in Lund Nano Lab by Pradheebha Surendiran. For LMs in these channels, we got $\alpha > 1.2$ for a few observed motors in 2.2 μm wide channels but remaining around 1 for most of them (Figure 6b).

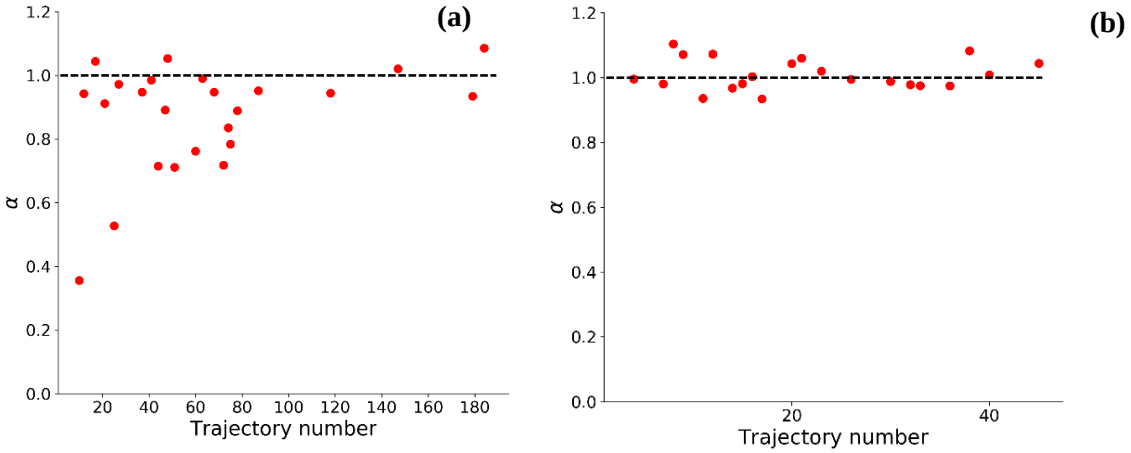

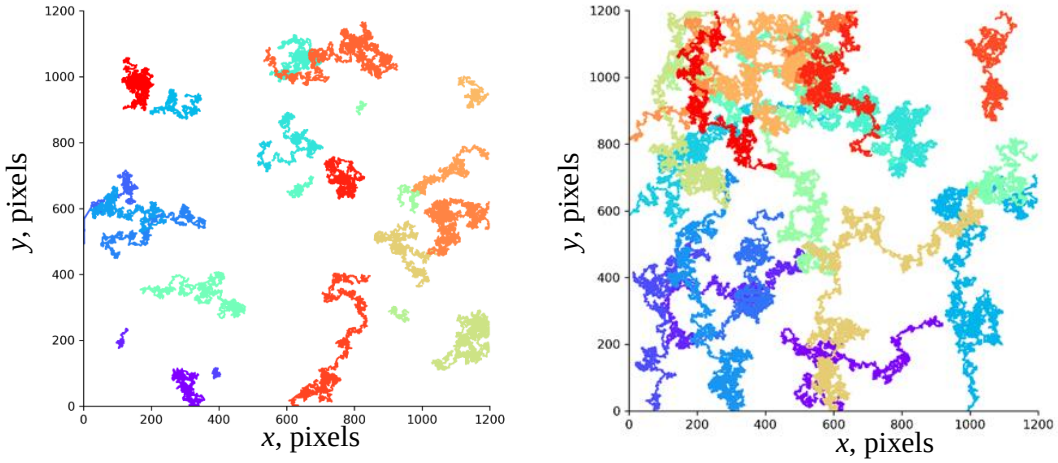

Figure 5. α coefficients (first row) and trajectories (second row) of LMs on (a) peptide lawn; (b) no-peptide substrate. The α's are calculated from TA MSDs, maximum time lag τ is 0.1 of the total duration of a trajectory.

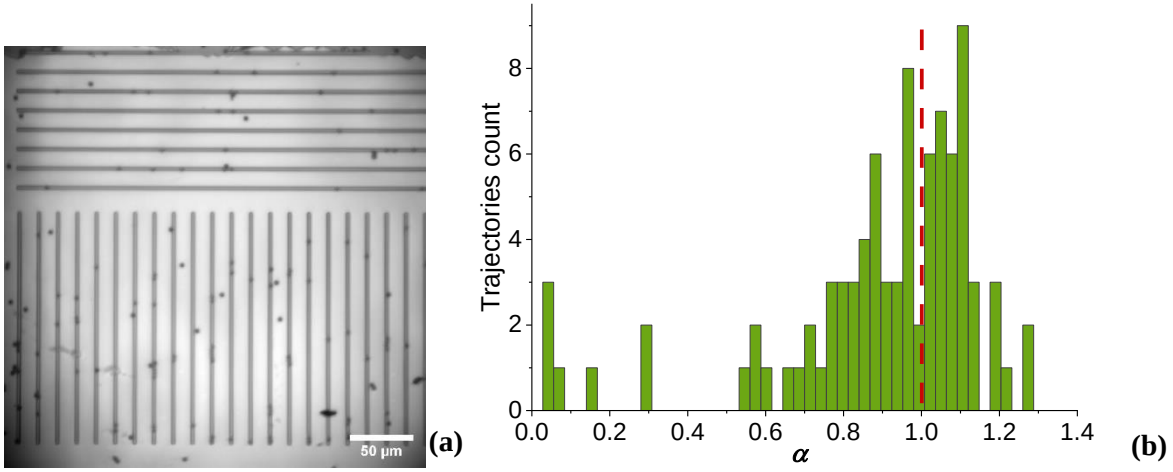

Figure 6. (a) LMs (dark dots) in channels on SiO2. The channels were fabricated by Pradheebha Surendiran using electron beam lithograpy in resist-coated SiO_2. (b) Distribution of α coefficients for LMs in 2.2 μm wide channels. The α's are calculated from TA MSDs, maximum time lag τ is 0.1 of the total duration of a trajectory.

3.2. Tumbleweed

We attempted observing labelled TWs on tracks attached to a micron sized bead, so that the fluorescence from multiple motors forms a circular pattern around the bead (Figure 7a). The radius of this circle (Figure 7b) can be localized with a subdiffraction accuracy (< 10 nm), similarly to how it is done in cell surface optical profilometry [55]. However, detection of single steps of the motors was ultimately not successful due to unspecific binding of TWs to the beads and surrounding substrate.

To minimize unspecific surface binding of the motors, we have tested several coatings for glass. On sonicated (in ethanol and 1M NaOH) and plasma cleaned glass, we applied PLL-PEG, and, as an alternative, Sigmacote with Pluronic F-127[53]. Additionally, we applied 5% Tween 20 treatment. We found that the best protection is provided by PLL-PEG, however some TWs still bind to the surface.

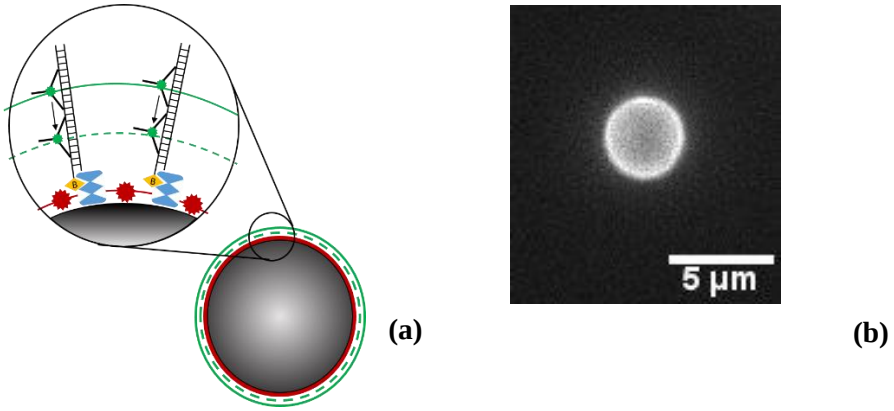

Figure 7. (a) Detection of TW motors steps on DNAs attached to a bead by circles of fluorescence (in green). Radius of the circle of fluorescence around the bead (in green) was expected to be localized with subdiffraction accuracy, thus showing where are the motors; when they step towards the bead the circle would narrow. (b) Fluorescent signal from motors on DNAs on a bead.

3.3. NWs in molecular motor studies

For the future, we propose to observe the sub-diffraction steps of Tumbleweed using semiconductor NWs. Previously, gallium phosphide (GaP) NWs have been used to track actins moving up and down the vertical NWs by the change in fluorescence intensity observed from above (Figure 8a).[25] This method allows for seeing larger scale motions (Figure 8b, 8c), but it cannot achieve the accuracy which would be enough to see the moving TW.

The approach we propose is discussed further in this thesis and relies on the results we obtained when optimizing the dimensions of NWs for excitation enhancement, which are described below.

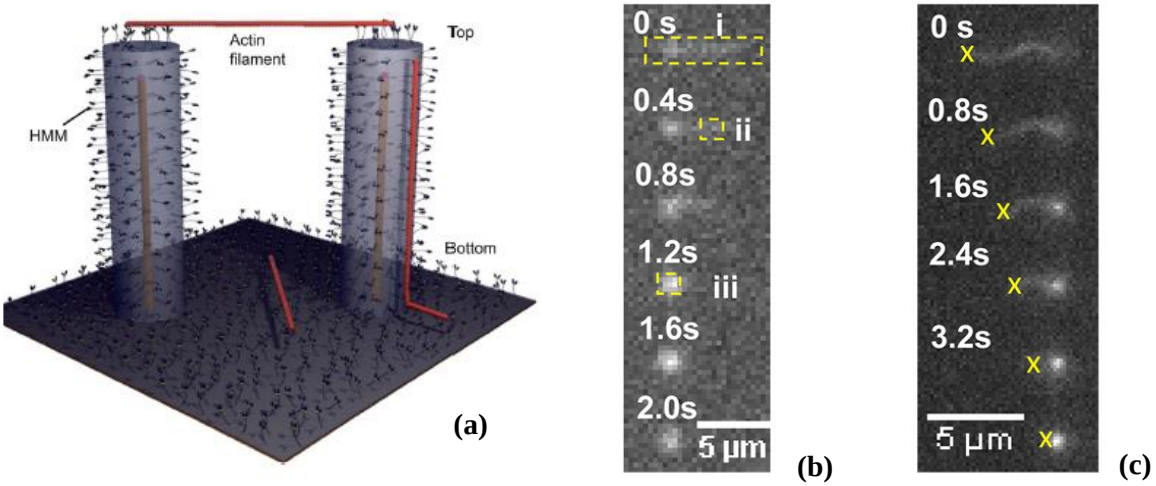

Figure 8. (a) Fluorescent actin filaments moving across a heavy meromyosins (HMM) functionalized substrate and onto GaP NWs. (b) Fluorescence of a filament climbing down a NW, (c) up a NW. *Reproduced from ref. [25] with permission from American Chemical Society.*

Chapter 4. Fluorescence waveguiding and enhancement in GaP nanowires. Fluorescent metal nanostructures.

4.1. NWs and lightguiding

For use in biosensing, nanowires (NWs) (Figure 9) have advantages such as high aspect ratio, controllable dimensions, suitability for surface modifications. In addition, the high refractive index *n* of semiconductor

materials such as GaP (n > 3.1 for visible light), which is also transparent for wavelengths of 570-1100 nm, facilitates optical waveguiding (lightguiding), when light propagates along the NWs and hence can be re-emitted from their tips. Guiding of light may be used for biosensing[23,24,56], trapping the light[57], and characterization of diffusion in lipid bilayers[22]. Waveguiding n nanowires is also often studied for lasing, as a nanowire waveguide with cleaved ends presents a Fabry–Pérot cavity. [58–62]

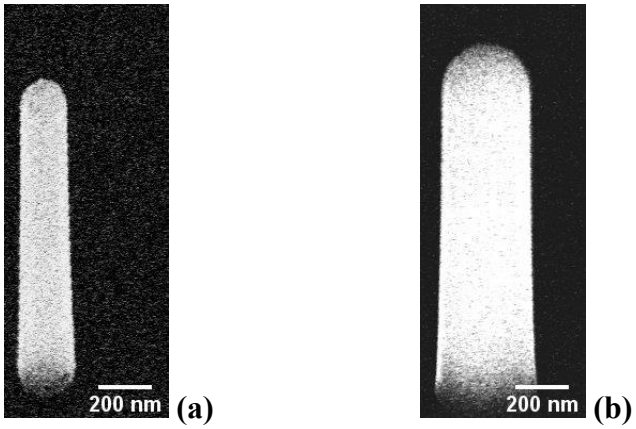

Figure 9. SEM image of vertical NWs with Al_2O_3 thickness (a) 30 nm, (b) 115 nm on GaP substrate under 30° to the surface (both NWs have d = 109 ± 10 nm).

Lightguiding NWs have been considered as optical fibers which means that there exist waveguide modes corresponding to optical resonances.[63,64] As in a fiber, number of waveguide modes depends on normalized optical frequency $V = \pi \frac{d}{\lambda} \sqrt{n_1^2 - n_0^2}$ where d – diameter of the wire, λ – wavelength, n_1 and n_0 – refractive indexes of NW core and surrounding media respectively[65]; a fiber is single-mode at V < 2.4. In GaP NWs, light guidance was found when V > 2 (Figure 10a, 10b), which indicates that higher order waveguide modes facilitate lightguiding: local peaks in power coupled into the NWs were attributed, in addition to the one due to the fundamental HE11 wavegiuding mode, to the TE01 mode, combination of HE21,TM01 and EH11, combination of HE12, HE31 and EH21 and combination of TM02, TE02, and HE41 modes[23]. Importantly, coupling of light from fluorophores into waveguide modes of a NW is a near-field effect. Therefore, it ceases if the source of light (fluorophore) moves away from the NW's surface further than on 100 nm.

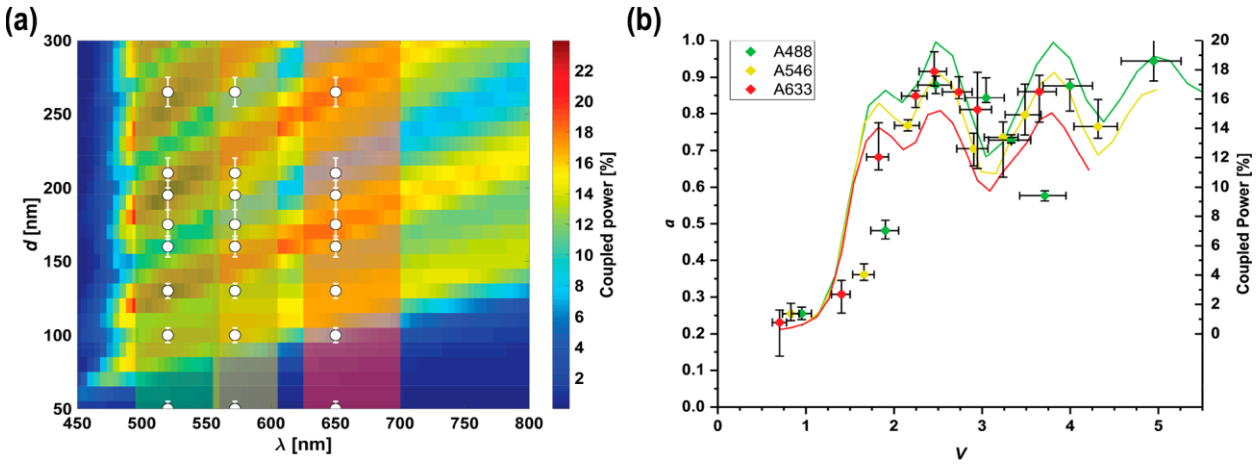

Figure 10. Dependence of power coupled with GaP NWs and asymmetry a (the extent of light emitted from the tip of a NW) on (a) wavelength and (b) normalized optical frequency V for three fluorescent dyes. *Reproduced from ref. [23] with permission from American Chemical Society.*

Additionally, the emitter type and location, as well as the polarization of emission, also affect fluorescence guiding. Emission extraction efficiency can be defined as $\eta_{ext} = P_{top}/P$, where P_{top} is power of emission from the nanowire tip into the air, and P is the total emission power (including emission to the substrate).[66] η_{ext} *is* higher at smaller radii, but at those radii there is a decrease in the Purcell factor $C_{\mathrm{Purcell}} = P/P_{semi}$ (here P_{semi} is emission power into a homogenous surrounding with the same refractive index as of the NW) (Figure 11). Therefore for to maximize the emission, a tradeoff between C_{Purcell} and $\eta_{ext}$is needed.[66] If nanowire dimensions are tailored to fit the emitter, the signal intensity is enhanced, as it was shown for quantum dots[67] .

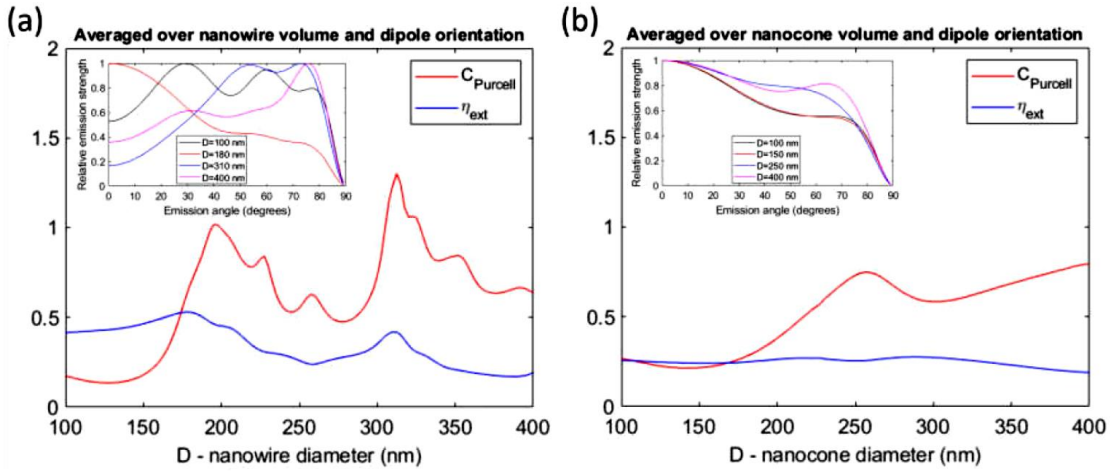

Figure 11. Emission extraction efficiency η_{ext} and Purcell factor C_{Purcell} for varied diameter of (a) a NW and (b) nanocone. *Reproduced under Open Access license from* [66].

4.2. Enhancement of fluorescence by NWs

Coupling of light from fluorophores located in proximity of a NW with the NW core is intertwined with fluorophore excitation enhancement, alteration in the radiative recombination rate of the fluorophore and emission directionality. For that reason, lightguiding in semiconductor NWs is often complemented by enhancement of fluorescence which is found in NWs and similar elongated structures of ZnO[68–72], Si[73] etc. The fluorescence enhancement has been recently described in [56,74–77]. Except for the aforementioned emission by a NW, the components of that enhancement have not been previously studied independently. In contrast, in NW based SERS systems the plasmonic excitation enhancement due to metal coated or metallic NWs is extensively studied and employed.[78–80]

As a part of the present work, fluorescence excitation enhancement has been studied as a stand-alone parameter, i.e. without the influence from the emission or recombination rate changes, using photobleaching. Total number of emitted photons by a fluorophore is $N = \frac{k_r}{k_b}$ where k_r and k_b – rates of radiative decay and irreversible photobleaching respectively.[81,82] Thus, N is independent of the excitation rate of the fluorophore but k_b is a function of excitation intensity.[83] Photobleaching may occur while fluorophores are in excited states, singlet and triplet ones.[84] Triplet state occurs once in about 1000 cycles, it is long-lived but not irreversible.[85] Detailed information about our study and its results follows in Section 4.3.

4.3. Relevance and methodology of our study on excitation enhancement by NWs

In the research article manuscript presented as a part of this thesis, we characterize one effect contributing to fluorescence guidance – the enhancement of excitation. The motivation for the study is that, to the best of our knowledge, no understanding has been achieved yet what dimension of NWs to choose to maximize excitation enhancement, although it has been demonstrated that the enhancement and lightguiding in NWs are diameter dependent[23,64,66]; therefore, knowing what diameters of NWs yield the best excitation enhancement, one can use those for applications.

We measure experimentally the excitation enhancement at varied diameter of NWs, and model the enhancement. We also measure and model how the enhancement depends on distance between fluorophores and a NW, which we vary by increasing the thickness of Al_2O_3 on the NWs. The modelling, done by Nicklas Anttu (Aalto University, Åbo Akademi University), is based on solving the Maxwell equations with a finite elements method.[86] Beyond just supporting our experimental results, the modelling shows how the enhancement changes with excitation wavelength and numerical aperture of the objective, thus expanding the findings to fluorophores and setups other than those we used for experiments. Below the methodology and results of the experimental part of the article are summarized, more detail on which are in the attached article manuscript.

The experimental contribution to this work is fluorescence microscopy of NWs. We used a popular red dye Alexa Fluor 647 (Thermo Fisher Scientific), but the results are immediately relevant for all other fluorophores with a similar excitation spectrum, since the system is defined by excitation wavelength exclusively. To estimate the enhancement, we use experimental photobleaching curves (Figure 12) to measure the photobleaching rate R of fluorophores on NWs (Figure 13a, 13b) from fitting with an exponent similar to that in [87]: $I(t) = Ae^{-Rt} + I_b$ where I_b – offset; R is independent on absolute intensities and thus does not require a calibration, For many NW samples bleaching deviates from a monoexponetial decay (Figure 12a), so for fluorophores on NWs we disregard the signal beyond first 100 s of bleaching for consistency of analysis.

For the diameters of NWs d = 70-230 nm with 10 nm of Al_2O_3 coating applied via atomic layer deposition (ALD), we calculate $M_{\mathrm{NW}} = \frac{dR}{dp}$ where p – excitation power, and $M_{\mathrm{NW}}/M_{\mathrm{Planar}}$ corresponds to the excitation enhancement on NWs relative to that on planar GaP coated with Al_2O_3.

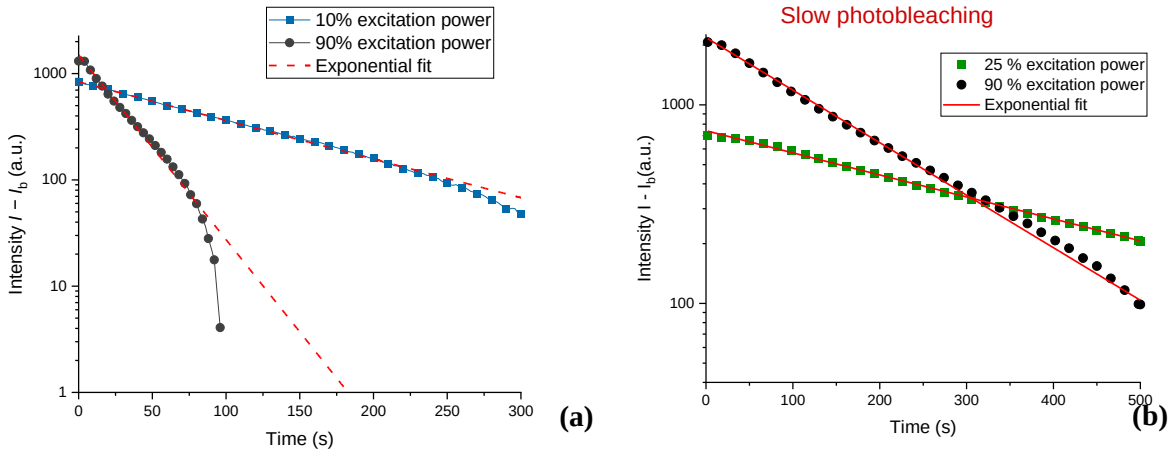

Figure 12. Typical photobleaching curves at varied excitation power at (a) D_{NW} = 109±10 nm, 10 nm Al_2O_3 coating; (b) GaP planar substrate.

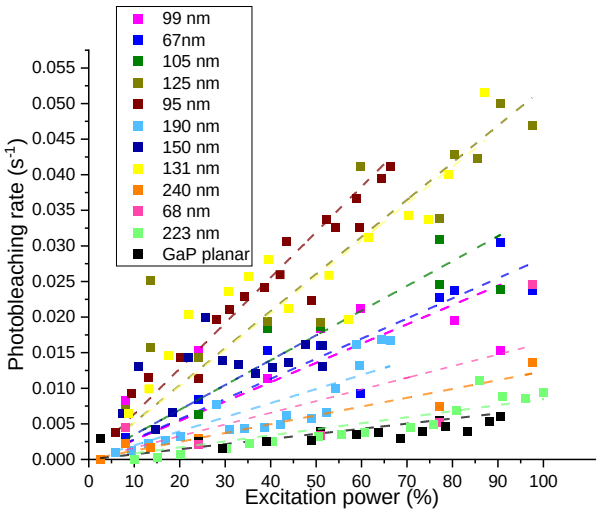

(a)

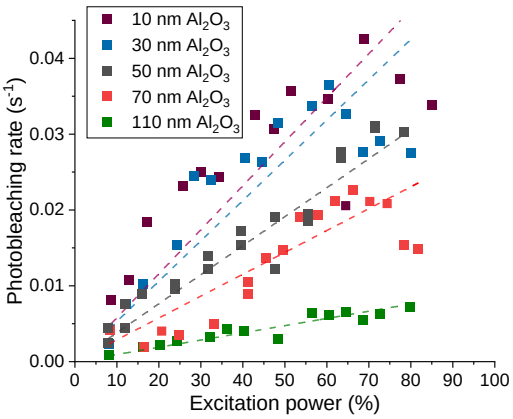

(b)

Figure 13. Photobleaching rates for: (a) planar GaP and NWs of varied diameter d (in legend), 10 nm Al_2O_3 coating; (b) d =109±10 nm with varied Al_2O_3 thickness (in legend).

4.4. Experimental results

We find that the enhancement $M_{\mathrm{NW}}/M_{\mathrm{Planar}}$ can be as large as a factor of five for d = 90-130 nm (Figure 14a). For the entire range d = 70-230 nm we find that $M_{\mathrm{NW}}/M_{\mathrm{Planar}} > 1$, which shows that all the studied NWs are enhancing the fluorescence compared to the signal on planar substrate. We also model $M_{\mathrm{NW}}/M_{\mathrm{Planar}}$, and find that the experimental result is in line with modelling, although the second peak that the modelling predicts at d = 210-220 nm was not resolved in the experiment, which may be due to changes in the position of that peak because of tapering of NWs (see Figure 9a) neglected in simulations. Furthermore, the modelling predicts that the peaks sequence is reshaped for shorter excitation wavelength (down to 450 nm), with the major peak shifting towards smaller diameters of NWs (Figure 14b).

At a fixed core diameter, we find that $M_{\mathrm{NW}}/M_{\mathrm{Planar}}$ decreases with increasing thickness of the Al_2O_3 coating t_{oxide} (Figure 15), which also agrees with our modelling and demonstrates the strongest enhancement when t_{oxide} does not exceed 10 nm. We attribute this to the difference of optical properties of Al_2O_3 (n=1.77 [88] for our excitation conditions) and GaP (n = 3.31[89]), due to which Al_2O_3 cannot support the coupling of light with the NW.

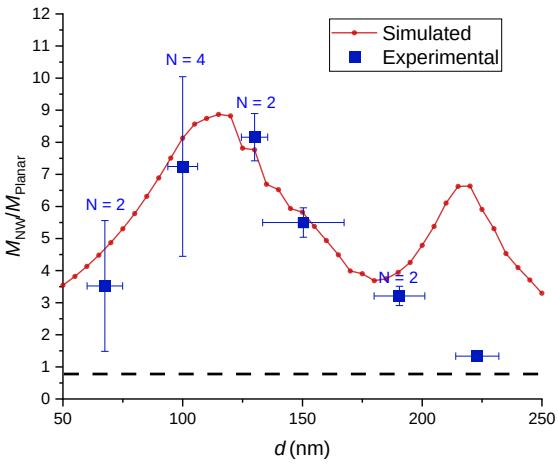

(a)

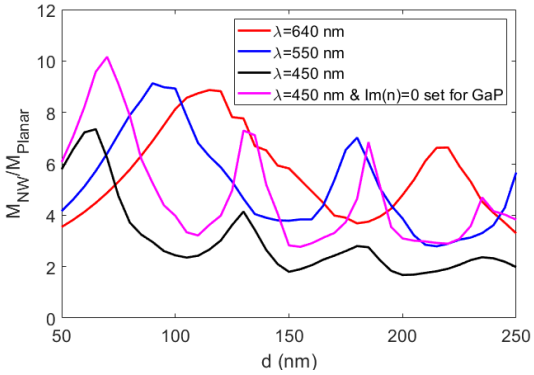

(b)

Figure 14. (a) Excitation enhancement on NWs of varied diameter with 10 nm of Al_2O_3. For experimental points marked with numbers $N > 1$, the result was averaged over N samples. (b) Modelled enhancement for varied excitation wavelength, NWs with 10 nm of Al_2O_3 were simulated.

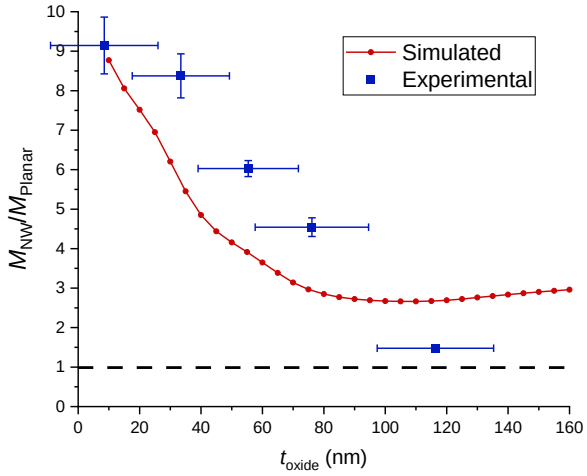

Figure 15. Excitation enhancement on NWs d = 109±10 nm at different t_{oxide}, thickness of Al_2O_3.

Chapter 5. Outlook and plans of further studies

5.1. Employing NWs to see Tumbleweed stepping

Our study demonstrates that only the fluorophores located at a distance <80 nm from the NW core are involved in lightguiding, and the excitation increases quickly as fluorophores are located closer to the NW core surface. Based on that, we suggest to observe the nanoscale motions of the Tumbleweed motor by using DNA tracks anchored with by one end to the NW surface (Figure 16a). The length of a track consisting of a full set of three binding sites (ABC, see Figure 3) together with the anchoring part is about 40 nm and thus comparable to the persistence length of the double stranded DNA (≈ 50 nm)[36]. Therefore, if necessary, the track can be built into a DNA origami for extra stability in order to help keep the DNA straightened, provided that the origami construct is sufficiently rigid as a whole. Already when the TW motor moves a few steps from the NW, its fluorescence would weaken, and its bleaching would slow down, since the excitation and emission enhancement induced by NW will be lost. Fluorescence will also no longer be emitted from the tip of the NW which could be seen from altered peak in point spread function (PSF). These changes in fluorescence can indicate if molecular motors are moving along the track towards or away from the NW. For a track walking molecular motor, one could see when the motor approaches the NW. An option for a short track is also to attach a FRET acceptor to the anchored end of the track (Figure 16b) so that a FRET pair is formed between donors on moving motors and the acceptor.

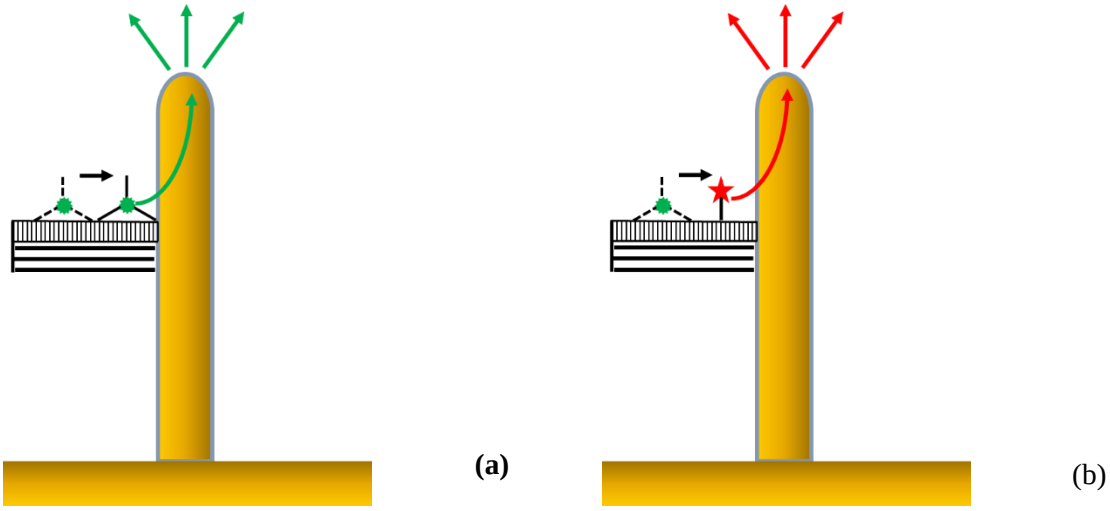

Figure 16. TW motors on DNA attached to a NW with (a) fluorescence for a label on TW being guided to the NW tip; (b) fluorescence is from a FRET acceptor on the DNA.

5.2. Calcium sensor based on NWs

Another potential application we propose for GaP NWs is a sensor for Ca^{2+} that would employ S100G, a protein to which Ca^{2+} ions bind. The domains of S100G assemble in presence of Ca^{2+}, and one of them may be attached to the NW surface. The other domain is planned to bear a fluorophore which would allow for detection of binding between the domains when there are the ions in the buffer.

5.3. Metal nanoclusters on nucleic acids as an alternative approach to fluorescence biosensors

An interesting class of biosensors is based on fluorescent noble metal nanoclusters (NC) on DNA. These were used for e.g. detection of Pb^{2+} and L-histidine using Ag NCs modified DNA molecular beacons and DNAzymes[90], ATP detection with Ag NCs containing DNA beacons [91], label-free detection of HIV-DNA by interaction between of NCs DNA and carbon nanoparticles[92]. Such NCs, containing 2-30 atoms[93], are formed because nucleobases, predominantly cytosine and guanine[94], can coordinate metal ions in presence of a reduction agent. The Ag NCs on a single stranded (ss-) DNA were first described in 2004[95] and since

then various NCs, mostly Ag and Au, have been drawing a lot of attention as unique fluorophores that are small yet offer good quantum yield, brightness, and photostability. Recent advances in this field are described in reviews [96,97]. The sequence specific formation of NCs with different colour has been achieved on ss-DNA[98]; when such DNA with NCs hybridizes with guanine rich complementary strand, the NCs fluorescence increases[99]. That is the principle behind DNA NCs molecular beacons for biosensing, the advantage of which over conventional beacons is that NCs eliminate the need in a fluorophore-quencher pair. Even though ss-DNA provides better access to the coordinating positions on nucleobases, it is possible to make NCs on ds-DNA as well[100], at a price of a lower quantum yield. DNA templated NCs or molecular beacons with NCs could be attached to GaP NWs which would enhance and guide NCs fluorescence.

5.4. Further studies on the physics of lightguiding

A further advancement of our study would be to study how NWs alter emission of fluorophores by affecting their radiative recombination rate r_{rad}. Provided that the respective quantum yield $\mathrm{QY} = \frac{r_{\mathrm{rad}}}{r_{\mathrm{rad}}+r_{\text{non-rad}}}$ is high, it would be possible to estimate from an experiment how r_{rad} changes, as on a NW $r_{\mathrm{rad,\,NW}} = C_{\mathrm{Purcell}} r_{\mathrm{rad}}$ For this experiment, it could be promising to use fluorescence lifetime imaging microscopy (FLIM), and a fluorophore with a high QY and relatively long lifetime.

Lifetime is affected by environment of fluorophore, including buffer, oxidation, FRET etc. but not by the concentration of fluorophores, as well as the parameters of setup, i.e. excitation and focal plane [101]. There are two types of FLIM, time domain (TD) and frequency domain (FD). In TD FLIM, cameras collect the signal for a varied time (gating) after the excitation, and the exponential decay of fluorescence is reconstructed to find the lifetime. The limitations of TD FLIM are slower acquisition due to a camera exposure time, and dynamic range which may not allow to measure lifetime in highly bright samples.[102] TD FLIM suits well for fluorophores with a long lifetime, unlike Alexa Fluor 647 dye we are currently using, which has lifetime of only 1 ns. A better option for FLIM to study the emission on NWs would be Alexa Fluor 488 dye with a lifetime of 4.1 ns and QY of 0.92; however, the excitation band of the 488 dye overlaps with the absorption of 50 nm Au particles used for nanowires growth, and the absorption of GaP. There are alternatives with lifetimes as long as 20 ns[103]. In FD FLIM, the sample is excited with a sinusoidal pulse, and lifetime is measured from the phase shift of the emission signal from the excitation. FD measurements can be the choice for the system of multiple fluorophores species with different lifetime.

Acknowledgements

I would like to acknowledge my supervisor Prof. Heiner Linke and co-supervisor Prof. Sara Linse for their support. I am also grateful to Drs. Nicklas Anttu, Damiano Verardo, Gerda Rentschler and Mercy Lard, Profs. Christelle Prinz and Fredrik Höök for their help in NWs studies; Chapin Korosec and Prof. Nancy Forde for support in the Lawnmower studies; Assoc. prof. Peter Jönsson, Dr. Roberta Davies, Prof. Paul Curmi, Assoc. Prof. Till Böcking and Dr. Cassandra Niman for support in the Tumbleweed studies. A huge thank you to our group: Pradheebha, Roman, Jingyuan, Jonatan, Julia, Ruby, Yang Chen, you all are the best! Special thanks to Dr. Jason Beech for his help with microscopy and other things in labs. NWs were grown and characterized in Lund Nano Lab (LNL), we are grateful to Peter Blomqvist, Sungyoun Ju, Natalia Volkova, George Rydnemalm and Anders Kvennefors for technical support. I also want to acknowledge Profs. Magnus Borgström, Jonas Tegenfeldt, Martin Magnusson and the members of their groups for useful discussions and help. Last but most important, I am immensely grateful to my parents for all their advice and support.

Our projects have received funding from Swedish Research Council (project numbers 2015-03824, 2019-02435, 2020-04226), the European Union's Horizon 2020 research and innovation programme under grant agreement No 732482 (Bio4Comp), NanoLund. I received financial support from UNSW as a Visiting Junior Research Fellow in October-December 2018.

References

(1) Wang, Z.; Hou, R.; Loh, I. Y. Track-Walking Molecular Motors: A New Generation beyond Bridge-Burning Designs. *Nanoscale* **2019**, *11* (19), 9240–9263. https://doi.org/10.1039/c9nr00033j.

(2) Blanchard, A. T.; Bazrafshan, A. S.; Yi, J.; Eisman, J. T.; Yehl, K. M.; Bian, T.; Mugler, A.; Salaita, K. Highly Polyvalent DNA Motors Generate 100+ PN of Force via Autochemophoresis. *Nano Lett.* **2019**, *19* (10), 6977–6986. https://doi.org/10.1021/acs.nanolett.9b02311.

(3) Bodas, D.; Khan-Malek, C. Hydrophilization and Hydrophobic Recovery of PDMS by Oxygen Plasma and Chemical Treatment-An SEM Investigation. *Sensors Actuators, B Chem.* **2007**, *123* (1), 368–373. https://doi.org/10.1016/j.snb.2006.08.037.

(4) Mofidi, S. M.; Nejat Pishkenari, H.; Ejtehadi, M. R.; Akimov, A. V. Locomotion of the C60-Based Nanomachines on Graphene Surfaces. *Sci. Rep.* **2021**, *11* (1), 2576. https://doi.org/10.1038/s41598-021-82280-7.

(5) Uhl, E.; Mayer, P.; Dube, H. Active and Unidirectional Acceleration of Biaryl Rotation by a Molecular Motor. *Angew. Chemie - Int. Ed.* **2020**, *59* (14), 5730–5737. https://doi.org/10.1002/anie.201913798.

(6) Linke, H.; Höcker, B.; Furuta, K.; Forde, N. R.; Curmi, P. M. G. Synthetic Biology Approaches to Dissecting Linear Motor Protein Function: Towards the Design and Synthesis of Artificial Autonomous Protein Walkers. *Biophysical Reviews*. 2020, pp 1041–1054. https://doi.org/10.1007/s12551-020-00717-1.

(7) Kovacic, S.; Samii, L.; Curmi, P. M. G.; Linke, H.; Zuckermann, M. J.; Forde, N. R. Design and Construction of the Lawnmower, an Artificial Burnt-Bridges Motor. *IEEE Trans. Nanobioscience* **2015**, *14* (3), 305–312. https://doi.org/10.1109/TNB.2015.2393872.

(8) Pena-Francesch, A.; Giltinan, J.; Sitti, M. Multifunctional and Biodegradable Self-Propelled Protein Motors. *Nat. Commun.* **2019**, *10* (1), 1–10. https://doi.org/10.1038/s41467-019-11141-9.

(9) Roke, D.; Wezenberg, S. J.; Feringa, B. L. Molecular Rotary Motors: Unidirectional Motion around Double Bonds. *Proc. Natl. Acad. Sci. U. S. A.* **2018**, *115* (38), 9423–9431. https://doi.org/10.1073/pnas.1712784115.

(10) Zhou, Q.; Chen, J.; Luan, Y.; Vainikka, P. A.; Thallmair, S.; Marrink, S. J.; Feringa, B. L.; Van Rijn, P. Unidirectional Rotating Molecular Motors Dynamically Interact with Adsorbed Proteins to Direct the Fate of Mesenchymal Stem Cells. *Sci. Adv.* **2020**, *6* (5). https://doi.org/10.1126/sciadv.aay2756.

(11) Kopperger, E.; List, J.; Madhira, S.; Rothfischer, F.; Lamb, D. C.; Simmel, F. C. A Self-Assembled Nanoscale Robotic Arm Controlled by Electric Fields. *Science* **2018**, *359* (6373), 296–301. https://doi.org/10.1126/science.aao4284.

(12) Thubagere, A. J.; Li, W.; Johnson, R. F.; Chen, Z.; Doroudi, S.; Lee, Y. L.; Izatt, G.; Wittman, S.; Srinivas, N.; Woods, D.; Winfree, E.; Qian, L. A Cargo-Sorting DNA Robot. *Science* **2017**, *357* (6356). https://doi.org/10.1126/science.aan6558.

(13) Shi, Z. T.; Hu, Y. X.; Hu, Z.; Zhang, Q.; Chen, S. Y.; Chen, M.; Yu, J. J.; Yin, G. Q.; Sun, H.; Xu, L.; Li, X.; Feringa, B. L.; Yang, H. B.; Tian, H.; Qu, D. H. Visible-Light-Driven Rotation of Molecular Motors in Discrete Supramolecular Metallacycles. *J. Am. Chem. Soc.* **2021**, *143* (1). https://doi.org/10.1021/jacs.0c11752.

(14) Xin, L.; Zhou, C.; Duan, X.; Liu, N. A Rotary Plasmonic Nanoclock. *Nat. Commun.* **2019**, *10* (1).

https://doi.org/10.1038/s41467-019-13444-3.

(15) Grill, K.; Dube, H. Supramolecular Relay-Control of Organocatalysis with a Hemithioindigo-Based Molecular Motor. *J. Am. Chem. Soc* **2020**, *142*, 26. https://doi.org/10.1021/jacs.0c09519.

(16) Romeo-Gella, F.; Corral, I.; Faraji, S. Theoretical Investigation of a Novel Xylene-Based Light-Driven Unidirectional Molecular Motor. *J. Chem. Phys.* **2021**, *154* (6), 064111. https://doi.org/10.1063/5.0038281.

(17) Gilissen, P. J.; White, P. B.; Berrocal, J. A.; Vanthuyne, N.; Rutjes, F. P. J. T.; Feringa, B. L.; Elemans, J. A. A. W.; Nolte, R. J. M. Molecular Motor-Functionalized Porphyrin Macrocycles. *Nat. Commun.* **2020**, *11* (1). https://doi.org/10.1038/s41467-020-19123-y.

(18) Stolz, S.; Gröning, O.; Prinz, J.; Brune, H.; Widmer, R. Molecular Motor Crossing the Frontier of Classical to Quantum Tunneling Motion. *Proc. Natl. Acad. Sci. U. S. A.* **2020**, *117* (26), 14838–14842. https://doi.org/10.1073/pnas.1918654117.

(19) Ni, J. S.; Zhang, X.; Yang, G.; Kang, T.; Lin, X.; Zha, M.; Li, Y.; Wang, L.; Li, K. A Photoinduced Nonadiabatic Decay-Guided Molecular Motor Triggers Effective Photothermal Conversion for Cancer Therapy. *Angew. Chemie - Int. Ed.* **2020**, *59* (28), 11298–11302. https://doi.org/10.1002/anie.202002516.

(20) Small, L. S. R.; Bruning, M.; Thomson, A. R.; Boyle, A. L.; Davies, R. B.; Curmi, P. M. G.; Forde, N. R.; Linke, H.; Woolfson, D. N.; Bromley, E. H. C. Construction of a Chassis for a Tripartite Protein-Based Molecular Motor. *ACS Synth. Biol.* **2017**, *6* (6), 1096–1102. https://doi.org/10.1021/acssynbio.7b00037.

(21) Bromley, E. H. C. C.; Kuwada, N. J.; Zuckermann, M. J.; Donadini, R.; Samii, L.; Blab, G. A.; Gemmen, G. J.; Lopez, B. J.; Curmi, P. M. G. G.; Forde, N. R.; Woolfson, D. N.; Linke, H. The Tumbleweed: Towards a Synthetic Protein Motor. *HFSP J.* **2009**, *3* (3), 204–212. https://doi.org/10.2976/1.3111282.

(22) Verardo, D.; Agnarsson, B.; Zhdanov, V. P.; Höök, F.; Linke, H. Single-Molecule Detection with Lightguiding Nanowires: Determination of Protein Concentration and Diffusivity in Supported Lipid Bilayers. *Nano Lett.* **2019**, *19* (9), 6182–6191. https://doi.org/10.1021/acs.nanolett.9b02226.

(23) Verardo, D.; Lindberg, F. W.; Anttu, N.; Niman, C. S.; Lard, M.; Dabkowska, A. P.; Nylander, T.; Månsson, A.; Prinz, C. N.; Linke, H. Nanowires for Biosensing: Lightguiding of Fluorescence as a Function of Diameter and Wavelength. *Nano Lett.* **2018**, *18* (8), 4796–4802. https://doi.org/10.1021/acs.nanolett.8b01360.

(24) Verardo, D.; Liljedahl, L.; Richter, C.; Agnarsson, B.; Axelsson, U.; Prinz, C. N.; Höök, F.; Borrebaeck, C. A. K.; Linke, H. Fluorescence Signal Enhancement in Antibody Microarrays Using Lightguiding Nanowires. *Nanomaterials* **2021**, *11* (1), 227. https://doi.org/10.3390/nano11010227.

(25) Ten Siethoff, L.; Lard, M.; Generosi, J.; Andersson, H. S.; Linke, H.; Månsson, A. Molecular Motor Propelled Filaments Reveal Light-Guiding in Nanowire Arrays for Enhanced Biosensing. *Nano Lett.* **2014**, *14* (2), 737–742. https://doi.org/10.1021/nl404032k.

(26) Peng, H.-I.; Miller, B. L. Recent Advancements in Optical DNA Biosensors: Exploiting the Plasmonic Effects of Metal Nanoparticles. *Analyst* **2011**, *136* (3), 436–447. https://doi.org/10.1039/C0AN00636J.

(27) Andersson, T.; Bläckberg, A.; Lood, R.; Ertürk Bergdahl, G. Development of a Molecular Imprinting-Based Surface Plasmon Resonance Biosensor for Rapid and Sensitive Detection of Staphylococcus Aureus Alpha Hemolysin From Human Serum. *Front. Cell. Infect. Microbiol.* **2020**,

10. https://doi.org/10.3389/fcimb.2020.571578.

(28) Bazrafshan, A.; Meyer, T. A.; Su, H.; Brockman, J. M.; Blanchard, A. T.; Piranej, S.; Duan, Y.; Ke, Y.; Salaita, K. Tunable DNA Origami Motors Translocate Ballistically Over Mm Distances at Nm/s Speeds. *Angew. Chemie - Int. Ed.* **2020**, *59* (24), 9514–9521. https://doi.org/10.1002/anie.201916281.

(29) Yehl, K.; Mugler, A.; Vivek, S.; Liu, Y.; Zhang, Y.; Fan, M.; Weeks, E. R.; Salaita, K. High-Speed DNA-Based Rolling Motors Powered by RNase H. *Nat. Nanotechnol.* **2016**, *11* (2), 184–190. https://doi.org/10.1038/nnano.2015.259.

(30) Lund, K.; Manzo, A. J.; Dabby, N.; Michelotti, N.; Johnson-Buck, A.; Nangreave, J.; Taylor, S.; Pei, R.; Stojanovic, M. N.; Walter, N. G.; Winfree, E.; Yan, H. Molecular Robots Guided by Prescriptive Landscapes. *Nature* **2010**, *465* (7295), 206–209. https://doi.org/10.1038/nature09012.

(31) Samii, L.; Linke, H.; Zuckermann, M. J.; Forde, N. R. Biased Motion and Molecular Motor Properties of Bipedal Spiders. *Phys. Rev. E - Stat. Nonlinear, Soft Matter Phys.* **2010**, *81* (2). https://doi.org/10.1103/PhysRevE.81.021106.

(32) Pei, R.; Taylor, S. K.; Stefanovic, D.; Rudchenko, S.; Mitchell, T. E.; Stojanovic, M. N. Behavior of Polycatalytic Assemblies in a Substrate-Displaying Matrix. *J. Am. Chem. Soc.* **2006**, *128* (39), 12693–12699. https://doi.org/10.1021/ja058394n.

(33) Korosec, C. S.; Sivak, D. A.; Forde, N. R. Apparent Superballistic Dynamics in One-Dimensional Random Walks with Biased Detachment. *arXiv*. American Physical Society (APS) September 29, 2020, p 33520. https://doi.org/10.1103/physrevresearch.2.033520.

(34) Korosec, C. S.; Jindal, L.; Schneider, M.; Calderon de la Barca, I.; Zuckermann, M. J.; Forde, N. R.; Emberly, E. Substrate Stiffness Tunes the Dynamics of Polyvalent Rolling Motors. *Soft Matter* **2021**, *17* (6), 1468–1479. https://doi.org/10.1039/d0sm01811b.

(35) Korosec, C. S.; Zuckermann, M. J.; Forde, N. R. Dimensionality-Dependent Crossover in Motility of Polyvalent Burnt-Bridges Ratchets. *Phys. Rev. E* **2018**, *98* (3). https://doi.org/10.1103/PhysRevE.98.032114.

(36) Manning, G. S. The Persistence Length of DNA Is Reached from the Persistence Length of Its Null Isomer through an Internal Electrostatic Stretching Force. *Biophys. J.* **2006**, *91* (10), 3607–3616. https://doi.org/10.1529/biophysj.106.089029.

(37) Niman, C. S.; Beech, J. P.; Tegenfeldt, J. O.; Curmi, P. M. G.; Woolfson, D. N.; Forde, N. R.; Linke, H. Controlled Microfluidic Switching in Arbitrary Time-Sequences with Low Drag. *Lab Chip* **2013**, *13* (12), 2389. https://doi.org/10.1039/c3lc50194a.

(38) Schaufele, F.; Demarco, I.; Day, R. N. FRET Imaging in the Wide-Field Microscope. In *Molecular Imaging*; Elsevier Inc., 2005; pp 72–94. https://doi.org/10.1016/B978-019517720-6.50013-4.

(39) Arkin, M. R.; Glicksman, M. A.; Fu, H.; Havel, J. J.; Du, Y. *Inhibition of Protein-Protein Interactions: Non-Cellular Assay Formats*; Bethesda (MD): Eli Lilly & Company and the National Center for Advancing Translational Sciences, 2004.

(40) Bath, J.; Green, S. J.; Allen, K. E.; Turberfield, A. J. Mechanism for a Directional, Processive, and Reversible DNA Motor. *Small* **2009**, *5* (13), 1513–1516. https://doi.org/10.1002/smll.200900078.

(41) Green, S. J.; Bath, J.; Turberfield, A. J. Coordinated Chemomechanical Cycles: A Mechanism for Autonomous Molecular Motion. *Phys. Rev. Lett.* **2008**, *101* (23), 238101. https://doi.org/10.1103/PhysRevLett.101.238101.

(42) Shin, J. S.; Pierce, N. A. A Synthetic DNA Walker for Molecular Transport. *J. Am. Chem. Soc.* **2004**, *126* (35), 10834–10835. https://doi.org/10.1021/ja047543j.

(43) Wilson, M. R.; Solà, J.; Carlone, A.; Goldup, S. M.; Lebrasseur, N.; Leigh, D. A. An Autonomous Chemically Fuelled Small-Molecule Motor. *Nature* **2016**, *534* (7606), 235–240. https://doi.org/10.1038/nature18013.

(44) Von Delius, M.; Geertsema, E. M.; Leigh, D. A. A Synthetic Small Molecule That Can Walk down a Track. *Nat. Chem.* **2010**, *2* (2), 96–101. https://doi.org/10.1038/nchem.481.

(45) Martin-Fernandez, M. L.; Tynan, C. J.; Webb, S. E. D. A "pocket Guide" to Total Internal Reflection Fluorescence. *J. Microsc.* **2013**, *252* (1), 16–22. https://doi.org/10.1111/jmi.12070.

(46) Valero, J.; Pal, N.; Dhakal, S.; Walter, N. G.; Famulok, M. A Bio-Hybrid DNA Rotor-Stator Nanoengine That Moves along Predefined Tracks. *Nat. Nanotechnol.* **2018**, *13* (6), 496–503. https://doi.org/10.1038/s41565-018-0109-z.

(47) Tomov, T. E.; Tsukanov, R.; Glick, Y.; Berger, Y.; Liber, M.; Avrahami, D.; Gerber, D.; Nir, E. DNA Bipedal Motor Achieves a Large Number of Steps Due to Operation Using Microfluidics-Based Interface. *ACS Nano* **2017**, *11* (4), 4002–4008. https://doi.org/10.1021/acsnano.7b00547.

(48) Zhou, C.; Duan, X.; Liu, N. A Plasmonic Nanorod That Walks on DNA Origami. *Nat. Commun.* **2015**, *6*. https://doi.org/10.1038/ncomms9102.

(49) Wickham, S. F. J.; Endo, M.; Katsuda, Y.; Hidaka, K.; Bath, J.; Sugiyama, H.; Turberfield, A. J. Direct Observation of Stepwise Movement of a Synthetic Molecular Transporter. *Nat. Nanotechnol.* **2011**, *6* (3), 166–169. https://doi.org/10.1038/nnano.2010.284.

(50) Heath, G. R.; Scheuring, S. High-Speed AFM Height Spectroscopy Reveals Ms-Dynamics of Unlabeled Biomolecules. *Nat. Commun.* **2018**, *9* (1). https://doi.org/10.1038/s41467-018-07512-3.

(51) Heller, I.; Sitters, G.; Broekmans, O. D.; Farge, G.; Menges, C.; Wende, W.; Hell, S. W.; Peterman, E. J. G.; Wuite, G. J. L. STED Nanoscopy Combined with Optical Tweezers Reveals Protein Dynamics on Densely Covered DNA. *Nat. Methods* **2013**, *10* (9), 910–916. https://doi.org/10.1038/nmeth.2599.

(52) Olshausen, P. V.; Defeu Soufo, H. J.; Wicker, K.; Heintzmann, R.; Graumann, P. L.; Rohrbach, A. Superresolution Imaging of Dynamic MreB Filaments in B. Subtilis - A Multiple-Motor-Driven Transport? *Biophys. J.* **2013**, *105* (5), 1171–1181. https://doi.org/10.1016/j.bpj.2013.07.038.

(53) Kirkness, M. W. H.; Korosec, C. S.; Forde, N. R. Modified Pluronic F127 Surface for Bioconjugation and Blocking Nonspecific Adsorption of Microspheres and Biomacromolecules. *Langmuir* **2018**, *34* (45), 13550–13557. https://doi.org/10.1021/acs.langmuir.8b02877.

(54) Novotný, F.; Pumera, M. Nanomotor Tracking Experiments at the Edge of Reproducibility. *Sci. Rep.* **2019**, *9* (1). https://doi.org/10.1038/s41598-019-49527-w.

(55) Bakalar, M. H.; Joffe, A. M.; Schmid, E. M.; Son, S.; Podolski, M.; Fletcher, D. A. Size-Dependent Segregation Controls Macrophage Phagocytosis of Antibody-Opsonized Targets. *Cell* **2018**, *174* (1), 131-142.e13. https://doi.org/10.1016/j.cell.2018.05.059.

(56) Hahm, J. I. Zinc Oxide Nanomaterials for Biomedical Fluorescence Detection. *J. Nanosci. Nanotechnol.* **2014**, *14* (1), 475–486. https://doi.org/10.1166/jnn.2014.9099.

(57) Kim, H. M.; Park, J. H.; Lee, S. K. Fiber Optic Sensor Based on ZnO Nanowires Decorated by Au Nanoparticles for Improved Plasmonic Biosensor. *Sci. Rep.* **2019**, *9* (1).

https://doi.org/10.1038/s41598-019-52056-1.

(58) Duan, X.; Huang, Y.; Agarwal, R.; Lieber, C. M. Single-Nanowire Electrically Driven Lasers. *Nature* **2003**, *421* (6920), 241–245. https://doi.org/10.1038/nature01353.

(59) Huang, M. H.; Mao, S.; Feick, H.; Yan, H.; Wu, Y.; Kind, H.; Weber, E.; Russo, R.; Yang, P. Room-Temperature Ultraviolet Nanowire Nanolasers. *Science* **2001**, *292* (5523), 1897–1899. https://doi.org/10.1126/science.1060367.

(60) Mäntynen, H.; Anttu, N.; Lipsanen, H. Nanowire Oligomer Waveguide Modes towards Reduced Lasing Threshold. *Materials (Basel).* **2020**, *13* (23), 1–21. https://doi.org/10.3390/ma13235510.

(61) Li, C.; Wright, J. B.; Liu, S.; Lu, P.; Figiel, J. J.; Leung, B.; Chow, W. W.; Brener, I.; Koleske, D. D.; Luk, T. S.; Feezell, D. F.; Brueck, S. R. J.; Wang, G. T. Nonpolar InGaN/GaN Core-Shell Single Nanowire Lasers. *Nano Lett.* **2017**, *17* (2), 1049–1055. https://doi.org/10.1021/acs.nanolett.6b04483.

(62) Wu, C.; Wei, W.; Yuan, X.; Zhang, Y.; Yan, X.; Zhang, X. Design and Simulation of Low-Threshold Miniaturized Single-Mode Nanowire Lasers Combined with a Photonic Crystal Microcavity and Asymmetric Distributed-Bragg-Reflector Mirrors. *Nanomaterials* **2020**, *10* (12), 1–10. https://doi.org/10.3390/nano10122344.

(63) Seo, K.; Wober, M.; Steinvurzel, P.; Schonbrun, E.; Dan, Y.; Ellenbogen, T.; Crozier, K. B. Multicolored Vertical Silicon Nanowires. *Nano Lett.* **2011**, *11*, 1851–1856. https://doi.org/10.1021/nl200201b.

(64) Anttu, N. Geometrical Optics, Electrostatics, and Nanophotonic Resonances in Absorbing Nanowire Arrays. *Opt. Lett.* **2013**, *38* (5), 730. https://doi.org/10.1364/ol.38.000730.

(65) Gu, Z.; Song, Q.; Xiao, S. Nanowire Waveguides and Lasers: Advances and Opportunities in Photonic Circuits. *Frontiers in Chemistry*. Frontiers Media S.A. January 8, 2021, p 613504. https://doi.org/10.3389/fchem.2020.613504.

(66) Anttu, N.; Mäntynen, H.; Sorokina, A.; Kivisaari, P.; Sadi, T.; Lipsanen, H. Geometry Tailoring of Emission from Semiconductor Nanowires and Nanocones. *Photonics* **2020**, *7* (2). https://doi.org/10.3390/PHOTONICS7020023.

(67) Reimer, M. E.; Bulgarini, G.; Akopian, N.; Hocevar, M.; Bavinck, M. B.; Verheijen, M. A.; Bakkers, E. P. A. M.; Kouwenhoven, L. P.; Zwiller, V. Bright Single-Photon Sources in Bottom-up Tailored Nanowires. *Nat. Commun.* **2012**, *3* (1), 1–6. https://doi.org/10.1038/ncomms1746.

(68) Hu, W.; Liu, Y.; Zhu, Z.; Yang, H.; Li, C. M. Randomly Oriented ZnO Nanorods as Advanced Substrate for High-Performance Protein Microarrays. *ACS Appl. Mater. Interfaces* **2010**, *2* (6), 1569–1572. https://doi.org/10.1021/am100314w.

(69) Dorfman, A.; Kumar, N.; Hahm, J. Highly Sensitive Biomolecular Fluorescence Detection Using Nanoscale ZnO Platforms. *J. Phys. Chem. Solids* **2005**, *23* (7), 4890–4895. https://doi.org/10.1021/la053270.

(70) Hu, W.; Liu, Y.; Yang, H.; Zhou, X.; Li, C. M. ZnO Nanorods-Enhanced Fluorescence for Sensitive Microarray Detection of Cancers in Serum without Additional Reporter-Amplification. *Biosens. Bioelectron.* **2011**, *26* (8), 3683–3687. https://doi.org/10.1016/j.bios.2011.01.045.

(71) Du, B.; Tang, C.; Zhao, D.; Zhang, H.; Yu, D.; Yu, M.; Balram, K. C.; Gersen, H.; Yang, B.; Cao, W.; Gu, C.; Besenbacher, F.; Li, J.; Sun, Y. Diameter-Optimized High-Order Waveguide Nanorods for Fluorescence Enhancement Applied in Ultrasensitive Bioassays. *Nanoscale* **2019**, *11* (30),

14322–14329. https://doi.org/10.1039/c9nr02330e.

(72) Wang, T.; Centeno, A.; Darvill, D.; Pang, J. S.; Ryan, M. P.; Xie, F. Tuneable Fluorescence Enhancement of Nanostructured ZnO Arrays with Controlled Morphology. *Phys. Chem. Chem. Phys.* **2018**, *20* (21), 14828–14834. https://doi.org/10.1039/c8cp01493k.

(73) Zhao, X.; Alizadeh, M. H.; Reinhard, B. M. Harnessing Leaky Modes for Fluorescence Enhancement in Gold-Tipped Silicon Nanowires. *J. Phys. Chem. C* **2016**, *120* (37), 20555–20562. https://doi.org/10.1021/acs.jpcc.5b11702.

(74) Lard, M.; Linke, H.; Prinz, C. N. Biosensing Using Arrays of Vertical Semiconductor Nanowires: Mechanosensing and Biomarker Detection. *Nanotechnology* **2019**, *30* (21). https://doi.org/10.1088/1361-6528/ab0326.

(75) Hahm, J. I. Fundamental Properties of One-Dimensional Zinc Oxide Nanomaterials and Implementations in Various Detection Modes of Enhanced Biosensing. *Annu. Rev. Phys. Chem.* **2016**, *67*, 691–717. https://doi.org/10.1146/annurev-physchem-031215-010949.

(76) Myndrul, V.; Iatsunskyi, I. Nanosilicon-Based Composites for (Bio)Sensing Applications: Current Status, Advantages, and Perspectives. *Materials (Basel).* **2019**, *12* (18). https://doi.org/10.3390/ma12182880.

(77) Namdari, P.; Daraee, H.; Eatemadi, A. Recent Advances in Silicon Nanowire Biosensors: Synthesis Methods, Properties, and Applications. *Nanoscale Res. Lett.* **2016**, *11* (406). https://doi.org/10.1186/s11671-016-1618-z.

(78) Sinha, G.; Depero, L. E.; Alessandri, I. Recyclable SERS Substrates Based on Au-Coated ZnO Nanorods. *ACS Appl. Mater. Interfaces* **2011**, *3* (7), 2557–2563. https://doi.org/10.1021/am200396n.

(79) Fularz, A.; Almohammed, S.; Rice, J. H. Oxygen Incorporation-Induced SERS Enhancement in Silver Nanoparticle-Decorated ZnO Nanowires. *ACS Appl. Nano Mater.* **2020**, *3* (2), 1666–1673. https://doi.org/10.1021/acsanm.9b02395.

(80) Han, X. X.; Ji, W.; Zhao, B.; Ozaki, Y. Semiconductor-Enhanced Raman Scattering: Active Nanomaterials and Applications. *Nanoscale* **2017**, *9* (15), 4847–4861. https://doi.org/10.1039/c6nr08693d.

(81) Pellegrotti, J. V; Acuna, G. P.; Puchkova, A.; Holzmeister, P.; Gietl, A.; Lalkens, B.; Stefani, F. D.; Tinnefeld, P. Controlled Reduction of Photobleaching in DNA Origami−Gold Nanoparticle Hybrids. *Nano Lett.* **2014**, *14*, 17. https://doi.org/10.1021/nl500841n.

(82) Hirschfeld, T. Quantum Efficiency Independence of the Time Integrated Emission from a Fluorescent Molecule. *Appl. Opt.* **1976**, *15* (12), 3135. https://doi.org/10.1364/ao.15.003135.

(83) Song, L.; Hennink, E. J.; Young, I. T.; Tanke, H. J. Photobleaching Kinetics of Fluorescein in Quantitative Fluorescence Microscopy. *Biophys. J.* **1995**, *68* (6), 2588–2600. https://doi.org/10.1016/S0006-3495(95)80442-X.

(84) Eggeling, C.; Widengren, J.; Rigler, R.; Seidel, C. A. M. M. *Photobleaching of Fluorescent Dyes under Conditions Used for Single-Molecule Detection: Evidence of Two-Step Photolysis*; 1998; Vol. 70, pp 2651–2659. https://doi.org/10.1021/ac980027p.

(85) Ha, T.; Tinnefeld, P. Photophysics of Fluorescent Probes for Single-Molecule Biophysics and Super-Resolution Imaging. *Annual Review of Physical Chemistry*. 2012, pp 595–617. https://doi.org/10.1146/annurev-physchem-032210-103340.

(86) Anttu, N.; Mäntynen, H.; Sorokina, A.; Turunen, J.; Sadi, T.; Lipsanen, H. Applied Electromagnetic Optics Simulations for Nanophotonics. *J. Appl. Phys.* **2021**, *129* (13), 131102. https://doi.org/10.1063/5.0041275.

(87) Benson, D. M.; Bryan, J.; Plant, A. L.; Gotto, A. M.; Smith, L. C. Digital Imaging Fluorescence Microscopy: Spatial Heterogeneity of Photobleaching Rate Constants in Individual Cells. *J. Cell Biol.* **1985**, *100* (4), 1309–1323. https://doi.org/10.1083/jcb.100.4.1309.

(88) Dodge, M. J. "Refractive Index." In *Handbook of Laser Science and Technology, Volume IV, Optical Materials: Part 2*; Weber, M. J., Ed.; CRC Press: Boca Raton, 1986; p 30. https://doi.org/10.1201/9781003067955.

(89) Aspnes, D. E.; Studna, A. A. *Dielectric Functions and Optical Parameters of Si, Ge, GaP, GaAs, GaSb, InP, InAs, and InSb from 1.5 to 6.0 EV*; 1983; Vol. 27.

(90) Gong, L.; Kuai, H.; Ren, S.; Zhao, X. H.; Huan, S. Y.; Zhang, X. B.; Tan, W. Ag Nanocluster-Based Label-Free Catalytic and Molecular Beacons for Amplified Biosensing. *Chem. Commun.* **2015**, *51* (60), 12095–12098. https://doi.org/10.1039/c5cc04442a.

(91) Li, X.; Zhang, H.; Zhao, Y.; Lian, L.; Wang, X.; Gao, W.; Zhu, B.; Lou, D. Design and Synthesis of Ag Nanocluster Molecular Beacon for Adenosine Triphosphate Detection. *J. Anal. Methods Chem.* **2019**, *2019*. https://doi.org/10.1155/2019/2786156.

(92) Ye, Y. D.; Xia, L.; Xu, D. D.; Xing, X. J.; Pang, D. W.; Tang, H. W. DNA-Stabilized Silver Nanoclusters and Carbon Nanoparticles Oxide: A Sensitive Platform for Label-Free Fluorescence Turn-on Detection of HIV-DNA Sequences. *Biosens. Bioelectron.* **2016**, *85*, 837–843. https://doi.org/10.1016/j.bios.2016.06.001.

(93) Zheng, J.; Nicovich, P. R.; Dickson, R. M. Highly Fluorescent Noble-Metal Quantum Dots. *Annu. Rev. Phys. Chem.* **2007**, *58* (1), 409–431. https://doi.org/10.1146/annurev.physchem.58.032806.104546.

(94) Schultz, D.; Brinson, R. G.; Sari, N.; Fagan, J. A.; Bergonzo, C.; Lin, N. J.; Dunkers, J. P. Structural Insights into DNA-Stabilized Silver Clusters. *Soft Matter* **2019**, *15* (21), 4284–4293. https://doi.org/10.1039/c9sm00198k.

(95) Petty, J. T.; Zheng, J.; Hud, N. V.; Dickson, R. M. DNA-Templated Ag Nanocluster Formation. *J. Am. Chem. Soc.* **2004**, *126* (16), 5207–5212. https://doi.org/10.1021/ja031931o.

(96) Qiao, Z.; Zhang, J.; Hai, X.; Yan, Y.; Song, W.; Bi, S. Recent Advances in Templated Synthesis of Metal Nanoclusters and Their Applications in Biosensing, Bioimaging and Theranostics. *Biosensors and Bioelectronics*. Elsevier Ltd March 15, 2021. https://doi.org/10.1016/j.bios.2020.112898.

(97) New, S. Y.; Lee, S. T.; Su, X. D. DNA-Templated Silver Nanoclusters: Structural Correlation and Fluorescence Modulation †. *Nanoscale Rev. Cite this Nanoscale* **2016**, *8*, 17729. https://doi.org/10.1039/c6nr05872h.

(98) Sharma, J.; Yeh, H. C.; Yoo, H.; Werner, J. H.; Martinez, J. S. A Complementary Palette of Fluorescent Silver Nanoclusters. *Chem. Commun.* **2010**, *46* (19), 3280–3282. https://doi.org/10.1039/b927268b.

(99) Yeh, H. C.; Sharma, J.; Han, J. J.; Martinez, J. S.; Werner, J. H. A DNA-Silver Nanocluster Probe That Fluoresces upon Hybridization. *Nano Lett.* **2010**, *10* (8), 3106–3110. https://doi.org/10.1021/nl101773c.

(100) Li, W.; Liu, L.; Fu, Y.; Sun, Y.; Zhang, J.; Zhang, R. Effects of Polymorphic DNA on the

Fluorescent Properties of Silver Nanoclusters †. *Cite this Photochem. Photobiol. Sci* **2013**, *12*, 1864. https://doi.org/10.1039/c3pp50026h.

(101) Chen, L. C.; Lloyd, W. R.; Chang, C. W.; Sud, D.; Mycek, M. A. Fluorescence Lifetime Imaging Microscopy for Quantitative Biological Imaging. In *Methods in Cell Biology*; Academic Press Inc., 2013; Vol. 114, pp 457–488. https://doi.org/10.1016/B978-0-12-407761-4.00020-8.

(102) Datta, R.; Heaster, T. M.; Sharick, J. T.; Gillette, A. A.; Skala, M. C. Fluorescence Lifetime Imaging Microscopy: Fundamentals and Advances in Instrumentation, Analysis, and Applications. *J. Biomed. Opt.* **2020**, *25* (07), 1. https://doi.org/10.1117/1.jbo.25.7.071203.

(103) Chib, R.; Raut, S.; Shah, S.; Grobelna, B.; Akopova, I.; Rich, R.; Sørensen, T. J.; Laursen, B. W.; Gryczynski, Z.; Gryczynski, I. Fluorescence Studies of a Long Lifetime Fluorophore, ADOTA in Silica and PVA Thin Films. *Biophys. J.* **2015**, *108* (2), 623a. https://doi.org/10.1016/j.bpj.2014.11.3388.

Research article manuscript

Fluorescence excitation enhancement by waveguiding nanowires

Ivan Unksov[†, ‡], *Nicklas Anttu*[‖, ▽, ‡], *Damiano Verardo*[†], *Fredrik Höök*[◦], *Christelle Prinz*[†], *Heiner Linke*[*, †]

[†]NanoLund and Solid State Physics, Lund University, Box 118, 22100 Lund, Sweden

[‖]Department of Electronics and Nanoengineering, Aalto University, FI-00076 Aalto, Finland

[▽]Physics, Faculty of Science and Engineering, Åbo Akademi University, FI-20500 Turku, Finland

[◦]Department of Physics, Chalmers University of Technology, 41296 Gothenburg, Sweden

KEYWORDS. Nanowires, fluorescence, waveguiding, III−V, biosensing

[‡]These authors contributed equally

*Corresponding author: heiner.linke@ftf.lth.se

ABSTRACT. The optical properties of vertical semiconductor nanowires (NWs) allow for effective enhancement of the fluorescence signal from surface-bound fluorophores and have been proven to be useful in high-sensitivity biosensing. One of the major factors contributing to signal enhancement is thought to be the enhancement of the incident light at the positions of the

fluorophores, leading to a stronger fluorescence signal. Here, we combine light-scattering modelling with fluorescence photobleaching experiments to quantify the excitation enhancement in the optical near-field as a function of the distance between a fluorophore and NW sidewall. In agreement with the modeling results, we find that the photobleaching rate, indicative of the excitation light intensity, decreases within a few tens of nanometers from the NW sidewall. The enhancement is strongest for a certain range of NW diameters at a given excitation wavelength. Based on our experimentally validated model, we also predict that the excitation enhancement on NWs can be further enhanced by reducing the numerical aperture of the illumination objective. Our results help to quantitatively explain the observed fluorescence enhancement of NWs, and can be used to design NW-based optical systems for enhancing the incident light intensity for biosensing and other applications.

Semiconductor nanowires (NWs) can be used to enhance fluorescence signals and are thus promising systems for high-sensitivity optical biosensing. Such fluorescence signal enhancement has been demonstrated in a range of material systems, first for ZnO nanorods[1,2], and further found for similar nanostructures of ZnO[3–6], GaP[7,8], Si[9,10], InAs[11]. One contributing factor to the signal enhancement is a lightguiding effect, whereby light emitted by surface-bound fluorophores is guided to the NW tip, leading to emission localized at the tip, as demonstrated using SiO_2-coated GaP NWs [7,8,12] and ZnO nanorods [13,14]. The potential of fluorescent enhancement for high-sensitivity biosensing has been demonstrated in a number of biomolecular systems[15], including the use of ZnO NRs to detect human α-fetoprotein (AFP),[16] for label-free fluorescence detection of ATP[17] and for CEA biomarker fluorescence detection in sandwich immunoassays[5]. GaP NWs have been used for the single-molecule detection of proteins diffusing in supported lipid bilayers[18], and for the antibody-based detection of a range of protein biomarkers in low concentration in human serum.[8] The bioassay experiments[5,8] yielded an estimate of a total signal enhancement by a factor of 10-20 achievable with fluorophores bound to GaP NWs with wavelength-matching diameter, compared to fluorophores bound to a flat surface, consistent with an increased limit of detection by a factor of 10 observed using ZnO nanorods[5].

The lightguiding effect in NWs relies on the high refractive index of the NW material, together with an optimal NW diameter and a matching wavelength of emitted light.[12,19,20] These parameters define how many waveguide modes can be supported by the NW.[12,21] In general, a modification of a signal from a fluorophore due to the proximity of a NW is a complicated process that is predicted to include at least three separate optical effects: (1) The enhancement (or suppression) of excitation intensity at the location of the fluorophore, (2) the modification of the probability to

collect emitted photons, and (3) the modification of the radiative recombination rate of the fluorophore that affects the radiative yield of the fluorophore and hence detected signal intensity [22]. The overall fluorescence signal modification (as measured e.g. with fluorescent microscopy imaging) is then expected to depend on these three factors.

Excitation enhancement in surface-enhanced Raman scattering (SERS) has been extensively investigated [23–25] in metallic nanostructures. However, it has not been previously studied for fluorophores in the vicinity of semiconductor nanostructures.

Here, we study the modification of the fluorescence excitation intensity. We used vertical GaP NWs, chosen for exhibiting strong fluorescence enhancement due to their high refractive index (> 3.1 for visible light) and a low absorption coefficient for $\lambda > 460$ nm[26], which limits parasitic absorption of excitation light and fluorescence signal. Moreover, due to its indirect band gap, GaP does not exhibit any inherent photoluminescence, which otherwise could interfere with the signal from the fluorophores. A thin Al_2O_3 oxide layer was added to the GaP NWs to make it amenable to a large variety of surface functionalization schemes, and to be able to control the distance between the fluorophores and the NW surface.

We used the Maxwell equations to solve theoretically the scattering of light by the NWs and substrate, considering the numerical aperture (NA) of the illumination objective. The results allow us to predict the enhancement of the incident light intensity at the location of the fluorophores. The modelling predicts a clear peak in this excitation enhancement for a GaP NW diameter of 110 nm for the excitation wavelength of 640 nm (also used in our experiments). Our model also predicts a rapid drop in the excitation enhancement when increasing the Al_2O_3 oxide thickness on the surface of the GaP NW, which is the equivalent of moving the fluorophore further away from the sidewall of the NW.

In parallel, we introduce a method to study the near-field enhancement experimentally by measurements of the power dependent photobleaching rate of the fluorescence for different NW diameters and oxide thicknesses. Bleaching curves provide information about the state of fluorophores. This information is independent on the exact number of fluorophores in an observed location and does not require any absolute calibration of the signal level. As a reference, we use the bleaching rate of a planar samples to normalize for the inherent bleaching characteristics of the fluorophores, which are not included in the above optics modelling. The modification of the photobleaching rate in our experiments is expected to be directly proportional to the enhancement of the excitation at the location of the fluorophore. The experiments are in excellent quantitative agreement with the theoretical predictions, confirming the strong dependence of the excitation on the NW diameter, and the decay of the excitation enhancement with the distance to the NWs. Furthermore, we predict a strong effect on the excitation enhancement from the numerical aperture (NA) of the illumination objective. Our results contribute to quantitative understanding of the observed fluorescence enhancement by semiconducting NWs and can be used to optimize the NW dimensions for biosensing and other applications where signal enhancement is desirable.

Methods

Model for photobleaching

The rate of fluorophore photobleaching R increases with an excitation light intensity[27,28] and can thus be used to estimate the excitation intensity, provided that the increase is linear. In our experiments we confirmed that R increases linearly with the excitation power p (Figure S3c, S3d), indicating that we do not have any signal saturation. Therefore, the excitation enhancement provided by NWs can be obtained from measuring $M_{\mathrm{NW}}/M_{\mathrm{planar}}$, where $M_{\mathrm{NW}} =$

$\frac{dR_{\mathrm{NW}}}{dp}$, $M_{\mathrm{planar}} = \frac{dR_{\mathrm{planar}}}{dp}$, R_{NW} is the photobleaching rate for the fluorophores bound to NW's oxide coating, and R_{planar} is the corresponding rate on a planar reference sample.

Electromagnetic optics simulations

By modelling the electric field $|\mathbf{E}(\mathbf{r}_{\mathrm{fluor}})|^2$ induced by the incident light at the location $\mathbf{r}_{\mathrm{fluor}}$ of a fluorophore, we obtained the contribution of the excitation enhancement to the modification of the bleaching rate.

Briefly, we modeled the diffraction of incident light by solving the Maxwell equations with the finite-element method in Comsol Multiphysics, similarly as in [22]. The optical response of the constituent materials is described by their respective refractive indexes n. For GaP, we used n = 3.31[26] , for Al_2O_3 n=1.77 [29], and for surrounding media n = 1.33, which is the refractive index of water.

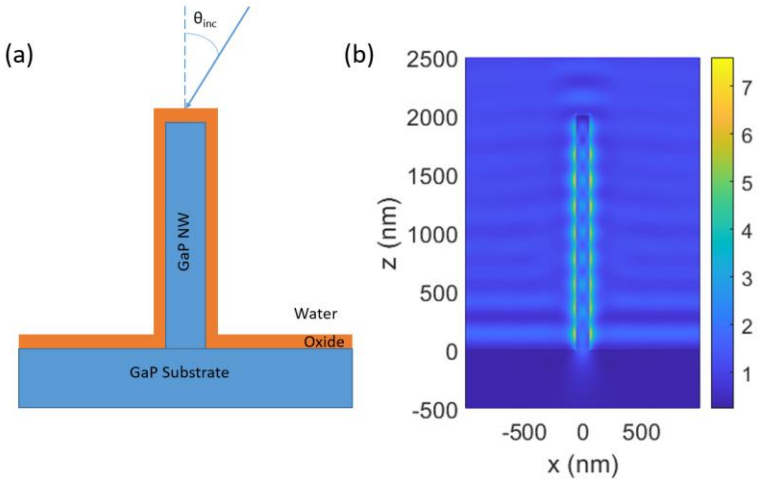

Figure 1. (a) Schematic of nanowire in modelling. (b) Modelled enhancement of the incident intensity for d = 110 nm, t_{oxide} = 10 nm, L = 2000 nm, NA = 1, and λ = 640 nm.

We modelled a single vertical NW of diameter d and length L standing on top of a semi-infinite GaP substrate, with a conformal Al_2O_3 oxide of thickness t_{oxide}, coating the surface of the NW and the substrate (see Figure 1). The modelling is done for the excitation wavelength λ = 640 nm,

corresponding to the laser wavelength used in the experiments. For the illumination in a widefield microscope, we assume incoherent light from all angles θ_{inc} within the NA of the illumination objective (that is, we consider $\theta_{inc} < \mathrm{asin}(NA/n)$ for the illumination). For a NA = 1 used in the experiments, and the surrounding water of $n = 1.33$, this corresponds to $\theta_{inc} < 49°$. We modelled the $|\mathbf{E}(\mathbf{r}_{fluor})|^2$ that an incident plane wave gives rise to, separately for each incident angle and for each of the two orthogonal polarization states. For the overall enhancement, we integrate over the contributing angles and both polarization states. This procedure results in a modelled excitation enhancement $\widetilde{M}_{\mathrm{NW}}(\mathbf{r}_{\mathrm{fluor}})$ for a given fluorescence position. By averaging over the axial position of the fluorophore on the nanowire sidewall, we obtain M_{NW}, the average enhancement for surface bound fluorophores, as compared to fluorophores located in water (without NW, oxide layer or substrate present). For a reference, we model also M_{Planar}, the variation in incident light intensity on a fluorophore located on top of an Al_2O_3 $t_{oxide} = 10$ nm planar layer deposited on a GaP substrate. We refer the reader to the Supporting Information (SI) for full technical details.

Nanowire growth and attachment of fluorophores

GaP nanowires were vertically grown using metalorganic vapour-phase epitaxy (MOVPE) seeded by 50 nm Au nanoparticles (see SI Section 1 for the growth details). For experiments at varied NW core diameter, we used NWs with L = 1.7-4.8 µm coated with t_{oxide} = 10 nm Al_2O_3 using ALD (Savannah S100, Cambridge NanoTech). When the Al_2O_3 thickness was varied, NW samples from a single growth were used, with d = 109 ± 10 nm, L = 1.7±0.2 µm (Figure S1). For the density and length of all the samples used in this study, see Figure S2a.

For functionalization with fluorophores, Al_2O_3 coated NWs were glued into flow channels (ibidi GmbH) (See SI Section 2) and washed with PBS buffer (P4417, Sigma-Aldrich), pH 6, then

incubated for 5 minutes with biotin-BSA (Sigma-Aldrich) 30 μM in PBS. Unbound BSA was then washed away from the chamber using PBS buffer, and the sample was incubated for 5 minutes with 50 μL of Alexa Fluor 647 streptavidin conjugate (S21374, ThermoFisher Scientific), 30 μM in PBS pH 7.2, in the dark. After washing off the excess of unbound dyes with PBS buffer, the samples were kept in the dark until imaging. Both surface functionalization and imaging were carried out at room temperature.

Microscopy and image analysis

For imaging, we used a Nikon TE2000-U microscope with a Nikon Fluor 60x/1.00w DIC water immersion objective (See Supporting Information Section 2 for setup details). For image analysis, we used ImageJ [30] with a custom script for correction for the lateral drift of a sample. We used Huang[31] or, typically for denser samples, Otsu[32] automatic thresholding for detection of sparsely located NWs (Figure S2b). We also applied additional restrictions on circularity and size of selected spots to select predominantly single NWs. Photobleaching curves were built using the average intensity in the detected areas in all frames. We fitted the curves with a monoexponential model similar to that in[33]: $I(t) = Ae^{-Rt} + I_b$, where R is a photobleaching rate, I_b is an offset. To exclude deviations from monoexponential decay observed in the longer time (Figure 2a), only the data from first 100 s of photobleaching were analyzed for consistency of analysis between all the NW samples. However, for fluorophores on a planar GaP, where bleaching is the slowest (Figure 2b), we observe less deviation from monoexponential decay compared to the NWs samples. Therefore, for the planar GaP reference sample we expand the time window to achieve better quality of the exponential fit and hence a more reliable value for R .

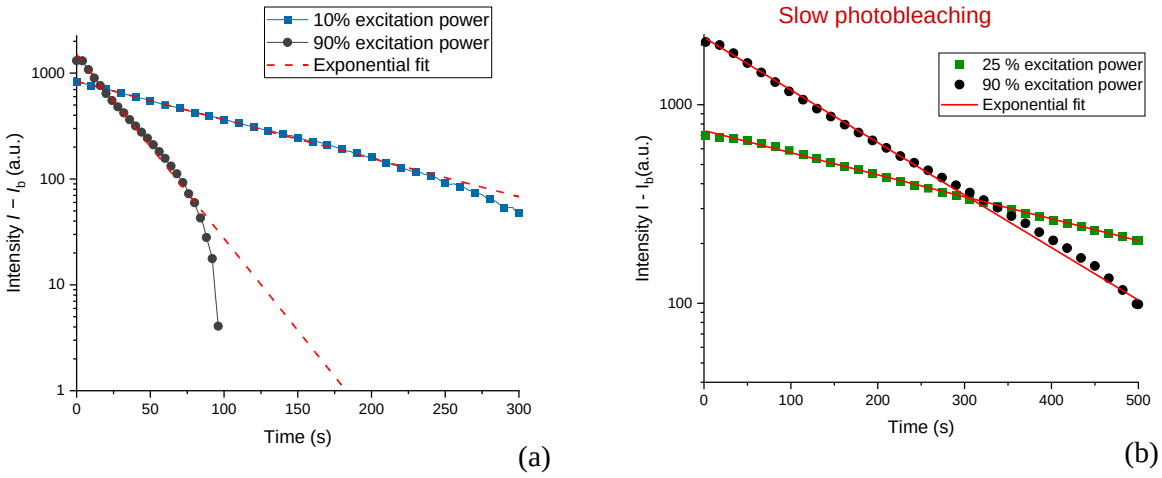

Figure 2. Typical photobleaching curves for two different excitation powers, for (a) a NW sample with $d = 109 \pm 10$ nm, $t_{oxide} = 10$ nm, and (b) a GaP planar substrate with the same t_{oxide}).

Results

Modelling

In Figure 3, we show the modelled ratio $\frac{M_{NW}}{M_{planar}}$ for varying d at fixed $t_{oxide} = 10$ nm, NA = 1, and $L = 2000$ nm, with $M_{planar} = 0.57$, such that ratios $\frac{M_{NW}}{M_{planar}} > 1.75$ correspond to an enhancement of excitation on the NW surface (compared to the fluorophore free in the liquid). For all considered d, we find that $\frac{M_{NW}}{M_{planar}} > 1$, starting from a value of 3.5 at the smallest $d = 50$ nm, with a peak of 8.9 at $d = 115$ nm. There is a second peak of $\frac{M_{NW}}{M_{planar}} = 6.6$ at $d = 220$ nm. When fixing $d = 110$ nm, that is, at the peak of $\frac{M_{NW}}{M_{planar}}$, and varying t_{oxide} (Figure 3), the model predicts a rapid drop from $\frac{M_{NW}}{M_{planar}} = 8.9$ at $t_{oxide} = 10$ nm to $\frac{M_{NW}}{M_{planar}} = 2.85$ at $t_{oxide} = 80$ nm. Such a rapid drop with

increasing distance away from the sidewall of the GaP NW is expected based on the spatially resolved enhancement of the incident intensity in the vicinity of the nanowire (Figure 1b and, for variation of t_{oxide}, Figure S9). From this spatially resolved enhancement, it is also expected that a variation of the nanowire length has only a minor effect on the enhancement: for L = 2000 nm, we find as many as nine interference lobes in the axial direction, and hence a variation of the NW length is expected to average over those multiple lobes. Indeed, in Supporting Information Figure S6, we found only weak dependence of the enhancement with varying L for L > 500 nm. As discussed in more detail in the Supporting Information (in connection to Supporting Information Figure S7), the peak that shows up at $d \approx 110$ nm and at $d \approx 220$ nm shifts linearly with varying the excitation wavelength (or more accurately, in a way that keeps the ratio $d_{\mathrm{peak}} n_{\mathrm{GaP}}(\lambda)/\lambda$ constant).

Experiments

When plotting R measured experimentally for different excitation powers, the slope is considered as the modification M of photobleaching rate, $M = \frac{dR(p)}{dp}$, where p is the excitation power (Figure S3c, S3d). The data obtained with different NWs batch of similar diameter (±10 nm) were averaged in Figure; the data without averaging are shown in **Error! Reference source not found.**S4. The measurements on NWs with fixed t_{oxide} = 10 nm (Figure3) show an enhancement $\frac{M_{\mathrm{NW}}}{M_{\mathrm{planar}}} > 5$ for diameters 90-140 nm, in good agreement with the predictions from the modelling. At all diameters of nanowires (70-240 nm) used in the experiments, we observed $\frac{M_{\mathrm{NW}}}{M_{\mathrm{planar}}} > 1$. We note that the modelling predicts a second, less-pronounced peak at d = 220 nm, which we did not observe experimentally.

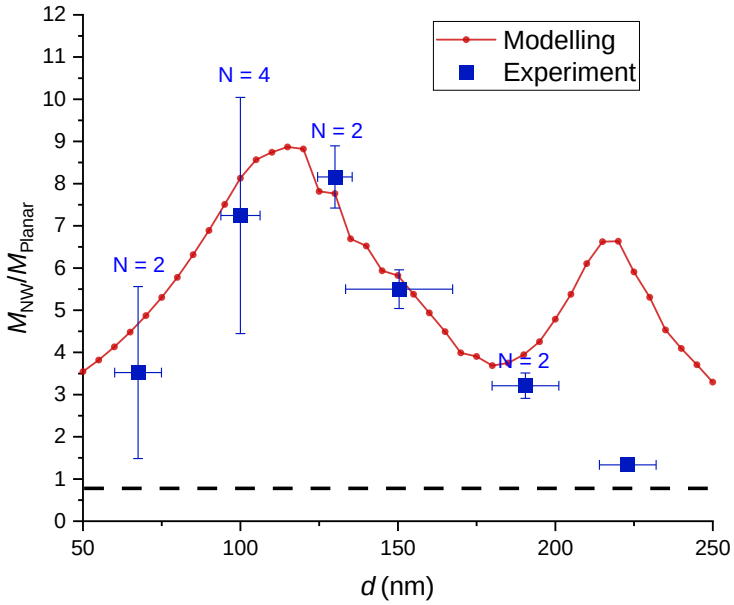

Figure 3. Experimental photobleaching rate enhancement and modelled excitation enhancement $M_{\mathrm{NW}}/M_{\mathrm{planar}}$ as a function of GaP NW core diameter d, for NA = 1, λ = 640 nm, t_{oxide} = 10 nm. Numbers $N > 1$ indicate where multiple close-lying data points for samples with similar diameter were averaged, and standard deviation was taken as the error where it exceeds the measurement error. (for the raw data, see Figure S4).

When increasing t_{oxide} for the NW core diameter at $d = 109 \pm 10$ nm, close to where we observed maximum enhancement, we measured a rapid decay of the enhancement with increasing t_{oxide} (Figure 4), which agrees with the modelling.

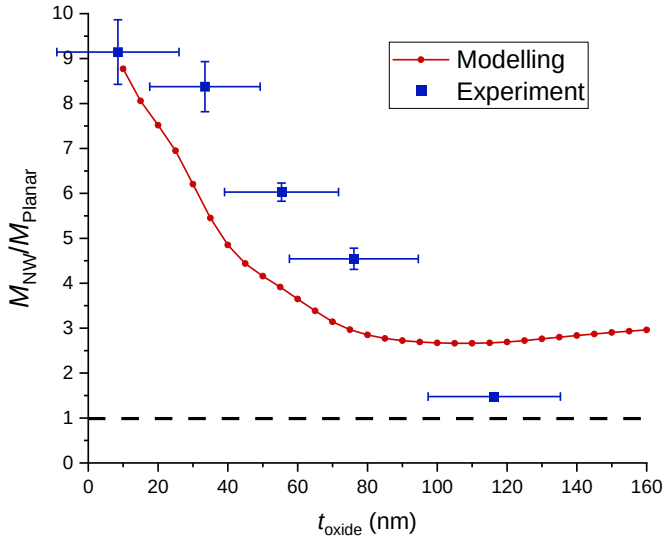

Figure 4. Normalized experimental photobleaching rate enhancement and modelled excitation enhancement for NA = 1 and λ = 640 nm as a function of t_{oxide} (the normalization is performed with M_{planar} for 10 nm oxide thickness). For the experiments, we used GaP NWs with d =109 ± 10 nm. For the modelling, we assumed a fixed d = 110 nm.

Modelling of auxiliary effects

Now that we have validated the modelling approach by the good agreement with experiments, we extend the study by additional modelling investigations. By varying the NA, we find that the modelled $M_{\text{NW}}/M_{\text{Planar}}$ is expected to strongly increase with decreasing NA at the peak at d = 115 nm (Figure 5). By moving to NA = 0.05, we predict an increase to $\frac{M_{\text{NW}}}{M_{\text{Planar}}} = 42$ from the $\frac{M_{\text{NW}}}{M_{\text{Planar}}} = 8.9$ at NA = 1, that is, an increase by a factor of 5. This enhancement is partly due to the decrease in M_{Planar} from 0.57 to 0.39 and partly due to an increase from 5.1 to 16.4 in M_{NW}. Thus, at this peak, the NW and planar surface show opposite tendencies in the field enhancement with decreasing NA. The planar surface shows increased partial destructive interference between

incident and reflected light, which decreases the electric field strength just above the surface. This destructive interference works more efficiently for normally incident light compared to light incident from a distribution of angles. In the case of NWs, in contrast, at the peak at $d \approx 110$ nm, it appears that the field enhancement is dominated by light incident from a narrow cone close to normal incidence, as supported by Figure S8 for angle-resolved field enhancement. Thus, with the peak at d ≈ 110 nm, by decreasing the NA, we can increase the relative excitation of fluorophores at NW sidewall compared to fluorophores on the planar oxide surface between the nanowires or free in the liquid (we note that in contrast, the peak at d ≈ 220 nm disappears as the NA is decreased (Figure 5): Indeed, from Figure S8, we find that for this peak the contribution to the enhancement originates from larger angles, which are filtered out by decreasing the NA.

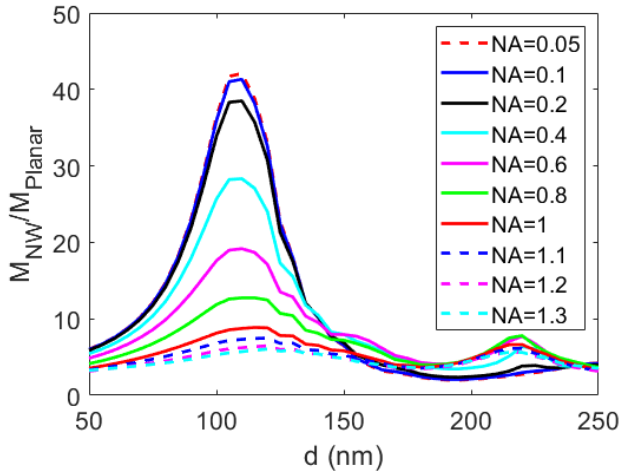

Figure 5. Modelled $M_{\mathrm{NW}}/M_{\mathrm{planar}}$ for $L = 2000$ nm at λ = 640 nm, varying NA, and t_{oxide} = 10 nm. The simulations are performed with a step of 5 nm in d. Here, M_{planar} decreases from 0.57 to 0.39 as NA is decreased from 1.3 to 0.05.

Such tailoring of the NA to enhance the excitation around the nanowire sidewall has the potential of reducing parasitic signal from unbound fluorophores (through the increase in $M_{\mathrm{NW}}/M_{\mathrm{Planar}}$).

In addition, for a given laser power on a fixed illumination area, a smaller NA yields a stronger excitation of the fluorophores at the NW sidewall (through the increase in M_{NW}).

M_{NW} depends additionally on L (Figure S6), however the dependence on L is negligible when $L \geq 1.5\lambda$; such weak dependence on L is expected also from the regular interference-like pattern with rather short period along the nanowire axis in Figure 1b).

Furthermore, we show with modelling that when the excitation wavelength is shorter than 640 nm, the enhancement maxima shift in a predictable manner to smaller diameters (Figure S7), which is useful for lightguiding systems employing other wavelengths.

Conclusions

To conclude, we studied the dependence of excitation enhancement in oxide coated GaP NWs and found that diameters of 90-140 nm and oxide thickness of 10 nm maximize the enhancement for widely used red excitation wavelengths. Measurements of the photobleaching rate is demonstrated to be useful when comparing excitation between different samples without measuring absolute signals. The results are supported by finite element modelling of diffraction of incident light for fluorophores on planar surface and around NWs. We also simulate the dependence of excitation enhancement on NW length, excitation wavelength and NA of the objective. Importantly, we predict a strong increase in the enhancement with decreasing NA of the illumination objective, which has the potential of reducing parasitic signal from unbound fluorophores.

ASSOCIATED CONTENT

Supporting Information

Section 1. Nanowire growth

GaP (111)B wafers were used as growth substrates. The seeding particles were deposited on a GaP wafer from aerosol. MOVPE growth was carried out at an Aix 200/4 (Aixtron AG) and started with axial growth at 480 °C to reach a desired length, followed by radial growth at 600 °C to increase the NW diameter from 50 nm (the diameter after axial growth equals to that of the seed particle) to a desired value. Reagents for the growth are phosphine (PH_3), trimethylgallium ($Ga(CH_3)_3$) and HCl. The dimensions of NWs were measured with SEM Hitachi SU8010 (Hitachi Ltd).

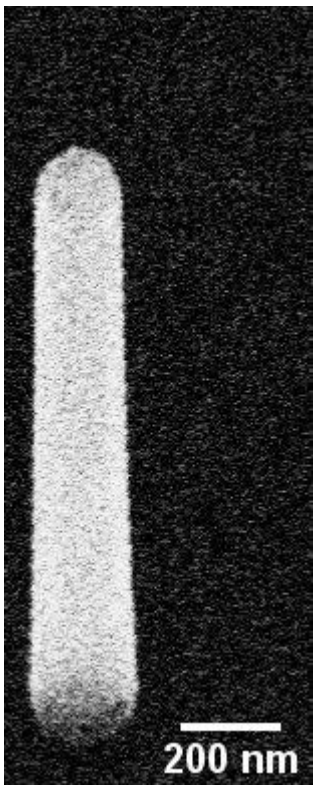

(a)

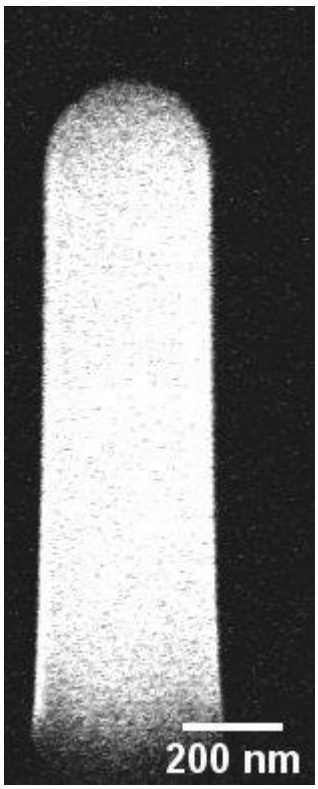

(b)

Figure S1. SEM image of vertical NWs with Al_2O_3 thickness (a) 30 nm, (b) 115 nm on GaP substrate under 30° to the surface (both nanowires have d = 109±10 nm).

Section 2. Sample preparation and imaging

For imaging, GaP substrates with NWs were glued with double-sided sticky tape in ibidi 6 channel slides and sealed with a glass coverslip (#1).

Nikon TE2000-U microscope was used with installed quad-band filterset (Semrock) and EMCCD camera Andor iXON Life 897 (Andor Oxford Instruments). Fluorescence was excited with OBIS 640nm LX 100mW laser. Prior to imaging, laser excitation intensity was routinely calibrated using power meter Thorlabs PM100D. In our data, 100 % excitation power corresponds to 350 μW as measured when the power meter is placed on top of the used objective, in the light path within the microscope.

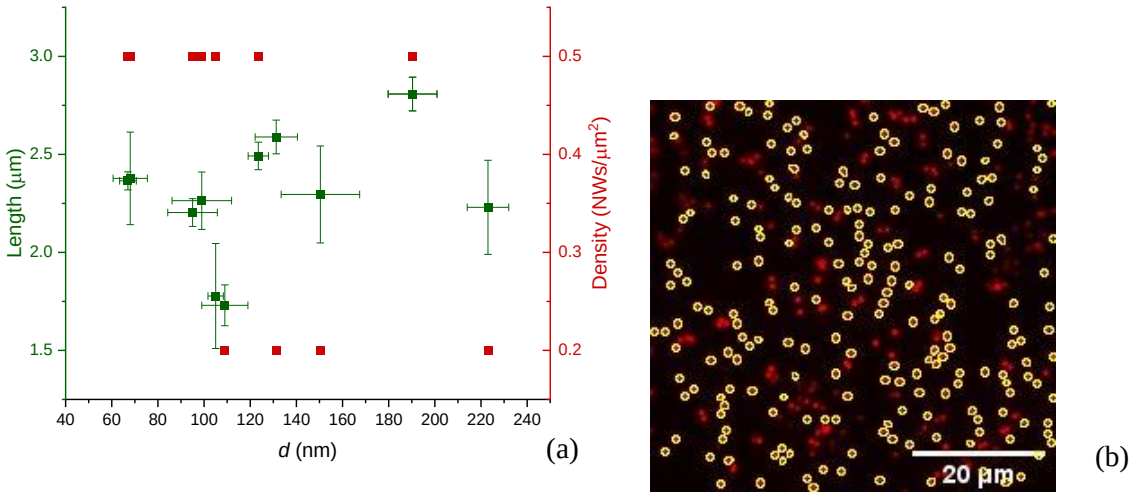

Figure S2. (a) Density and length of used NWs. (b) Fluorescence on NWs. In yellow – NW diffraction limited spot areas, average intensity from which was taken for the calculation of R.

Section 3. Power dependences of photobleaching rate

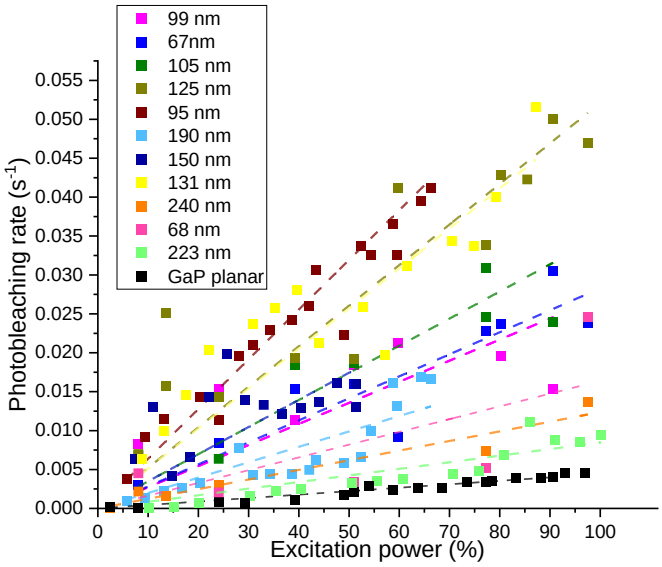

(a)

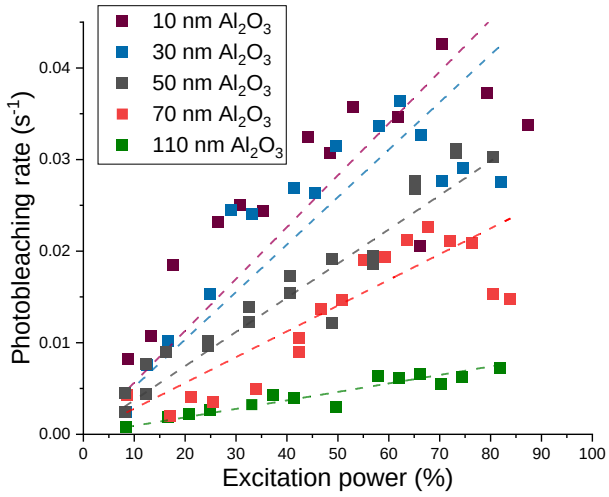

(b)

Figure S3. Photobleaching rates for (a) planar GaP and NWs of varied d, 10 nm Al_2O_3 coating; (b) d = 109±10 nm, varied Al_2O_3 thickness.

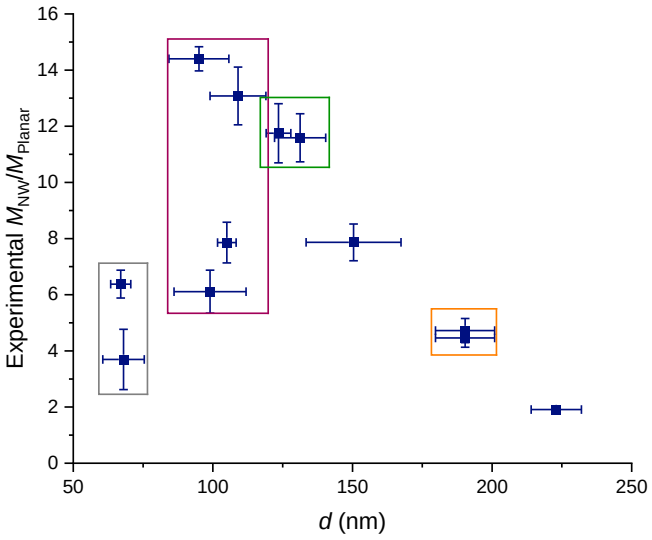

Figure S4. Experimental photobleaching rate enhancement before averaging of neighboring *d* datapoints (in rectangles).

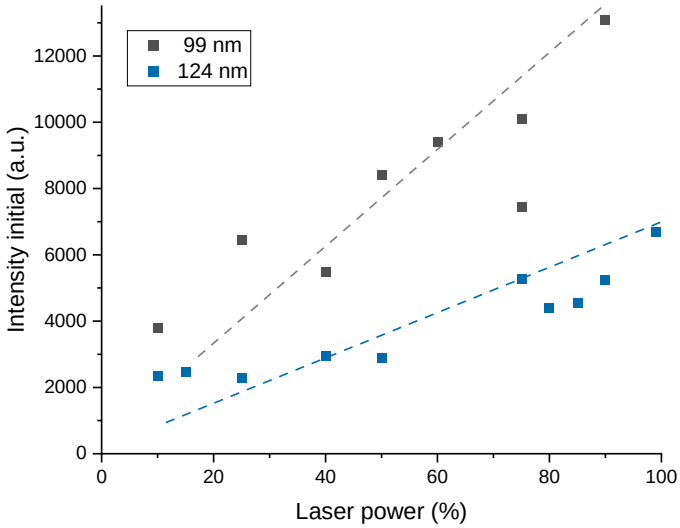

Figure S5. Fluorescence intensity at the onset of photobleaching at varied excitation power for two NW diameters.

Section 4. Additional technical details of optics modelling

We assume that the photo-excitation-de-excitation cycle of a fluorophore is dominated by the time it takes for a flurophore to get excited. Furthermore, we assume that the excitation probability of a fluorophore is proportional to the electric field strength squared, $|\mathbf{E}(r,z)|^2$, which shows circular symmetry for the circularly symmetric geometrical system and illumination condition (here, we have assumed that the excitation of the fluorophore does not show anisotropy with regard to the orientation of the local electric field). Thus, we assume that we are far from saturation in illumination power – this assumption we assessed experimentally by observing that the bleaching rate increase stays linear with increasing illumination power (Figure S5, saturation would show up as sublinear power dependence).

We model the diffraction of incident light by solving the Maxwell equations with the finite-element method in Comsol Multiphysics similarly as in [22].The optical response of the constituent materials is described by their respective refractive indexes *n*. For GaP, we use values from [26], for Al_2O_3 from[29], and for the surrounding water, we use $n = 1.33$.

We consider a plane wave at (vacuum) wavelength λ incident from a direction given by the polar angle θ_{inc} and azimuth angle ϕ_{inc} with polarization state *pol*. These incidence angles are defined such that $k_{z,inc} = k_0 n_{\mathrm{inc}} \cos(\theta_{\mathrm{inc}})$, $k_{x,inc} = k_0 n_{\mathrm{inc}} \sin(\theta_{\mathrm{inc}}) \cos(\phi_{\mathrm{inc}})$, and $k_{y,inc} = k_0 n_{\mathrm{inc}} \sin(\theta_{\mathrm{inc}}) \sin(\phi_{\mathrm{inc}})$. Here, n_{inc} is the (wavelength-dependent) refractive index in the medium from which light is incident from. For the polarization, we use two orthogonal states, chosen as *s* and *p* polarization here, where *s* polarization shows a zero value for the *z* component

of the electric field of the incident light (for the special case of $\theta_{\mathrm{inc}} = 0$ we choose s polarization to be an incident plane wave whose electric field is *y* polarized).

We use a scattered field formulation. There, we use as background field $\mathbf{E}_{\mathrm{bg}}(\mathbf{r}, \lambda, \theta_{\mathrm{inc}}, \phi_{\mathrm{inc}}, \mathrm{pol})$ the analytically known solution for the electric field for the case of a planar oxide layer on top of the substrate, that is, without the nanowire. In the simulations, we have chosen the magnitude of the electric field of the incident plane wave such that for given θ_{inc}, ϕ_{inc}, and pol it is 1 V/m. In more detail, we use the Fresnel coefficients at the top and the bottom interface of the oxide to create the solution, which includes the geometrical series within the oxide layer for the infinitely many round-trips of partial scattering within the oxide layer. Next, we include the nanowire as the scatterer and solve for the scattered field $\mathbf{E}_{\mathrm{sc}}(\mathbf{r}, \lambda, \theta_{\mathrm{inc}}, \phi_{\mathrm{inc}}, \mathrm{pol})$. Then, the total field is given by $\mathbf{E}(\mathbf{r}, \lambda, \theta_{\mathrm{inc}}, \phi_{\mathrm{inc}}, \mathrm{pol}) = \mathbf{E}_{\mathrm{bg}}(\mathbf{r}, \lambda, \theta_{\mathrm{inc}}, \phi, \mathrm{pol}) + \mathbf{E}_{\mathrm{sc}}(\mathbf{r}, \lambda, \theta_{\mathrm{inc}}, \phi_{\mathrm{inc}}, \mathrm{pol})$.

For the wide-field illumination, we assume incoherent plane waves from within the numerical aperture NA of the objective, with $\theta_{\mathrm{NA}} = \arcsin(\frac{\mathrm{NA}}{n_{inc}})$ the maximum incident angle, such that the intensity of the electric field at location $\mathbf{r}$ is given by:

$$|\mathbf{E}(\mathbf{r}, \lambda)|^2 = \sum_{\mathrm{pol}=s,p} \int_0^{\theta_{\mathrm{NA}}} \int_0^{2\pi} |\mathbf{E}(\mathbf{r}, \lambda, \theta_{\mathrm{inc}}, \phi_{\mathrm{inc}}, \mathrm{pol})|^2 \sin(\theta_{\mathrm{inc}}) d\phi_{\mathrm{inc}} d\theta_{\mathrm{inc}} / \sum_{pol=s,p} \int_0^{\theta_{\mathrm{NA}}} \int_0^{2\pi} \sin(\theta_{\mathrm{inc}}) d\phi_{\mathrm{inc}} d\theta_{\mathrm{inc}}. \quad (1)$$

With this choice for the normalization, $|\mathbf{E}(\mathbf{r}, \lambda)|^2 = 1 \left[\frac{\mathrm{V}}{\mathrm{m}}\right]^2$ corresponds to the same local intensity as on the fluorophore in the homogeneous liquid without nanowire, oxide, or substrate.

For the fluorophores around the nanowire, we consider

$$|\mathrm{E}(r, z, \lambda)|^2 = \int_0^{2\pi} |\mathbf{E}(x, y, z, \lambda)|^2 \, d\phi/(2\pi) \quad (2)$$

where $x = r\cos(\text{ø})$ and $y = r\sin(\text{ø})$. Importantly, due to the circular symmetry of the nanowire, in the calculations, we can exchange this ø averaging into an averaging over ø already in Eq. (SI 1). Hence, a simulation for a given ø_{inc} gives all the information we need about the variation of the averaged field over the circumference of the nanowire at given *r* for all the possible incidence angles ø_{inc}. Thus, we need only to vary θ_{inc} and pol in the actual simulations. We performed the modelling with a step of 5 degrees in θ_{inc}, after initial test runs indicating that negligible differences occurred compared to a much finer, and computationally more costly, stepping at 1 degree.

For completeness, we introduce the terms $|\mathrm{E}_{\mathrm{NW}}(r,z)|^2$ and $\left|\mathrm{E}_{\mathrm{planar}}(z)\right|^2$ for a fluorophore in the vicinity of the nanowire and a flurophore on top of the planar substrate without the nanowire present.

In the modelling, we assume that the fluorophores reside in a Δ_{Fluor} = 10 nm wide layer, in water, on top of the oxide. We calculate then the bleaching rate modification, relative to the fluorophore in the liquid, as (note that the substrate/oxide interface is located at *z* = 0):

$$M_{\mathrm{NW}} = \frac{\int_{z=t_{\mathrm{oxide}}}^{z=t_{\mathrm{oxide}}+L}\int_{r=d/2+t_{\mathrm{oxide}}}^{r=d/2+t_{\mathrm{oxide}}+\Delta_{\mathrm{Fluor}}}|\mathrm{E}_{\mathrm{NW}}(r,z)|^2 r\,dr\,dz}{L[(d/2+t_{\mathrm{oxide}}+\Delta_{\mathrm{Fluor}})^2-(d/2+t_{\mathrm{oxide}})^2]/2}$$

$$M_{\mathrm{Planar}} = \frac{\int_{z=t_{\mathrm{oxide}}}^{z=t_{\mathrm{oxide}}+\Delta_{\mathrm{Fluor}}}\left|\mathrm{E}_{\mathrm{planar}}(z)\right|^2 dz}{\Delta_{\mathrm{Fluor}}}$$

Then, from $M_{\mathrm{NW}}/M_{\mathrm{Planar}}$ we obtain the value to compare with experiments. Importantly, when we use $M_{\mathrm{NW}}/M_{\mathrm{Planar}}$ to quantify the bleaching rate modification, we do not need to know the

actual illumination power or the bleaching rate in the test liquid for a given illumination power. Therefore, $M_{\mathrm{NW}}/M_{\mathrm{Planar}}$ is independent of the exact choice of the fluorophore, as long as it can be excited at λ and the fluorescence is detected by our optical system.

Note that M_{NW} depends on r_{NW} and t_{oxide} (also on L but that dependence is insignificant for $L \geq 1.5\lambda$, see Figure S6) , and M_{Planar} depends on t_{oxide}; furthermore, both depend on λ and NA.

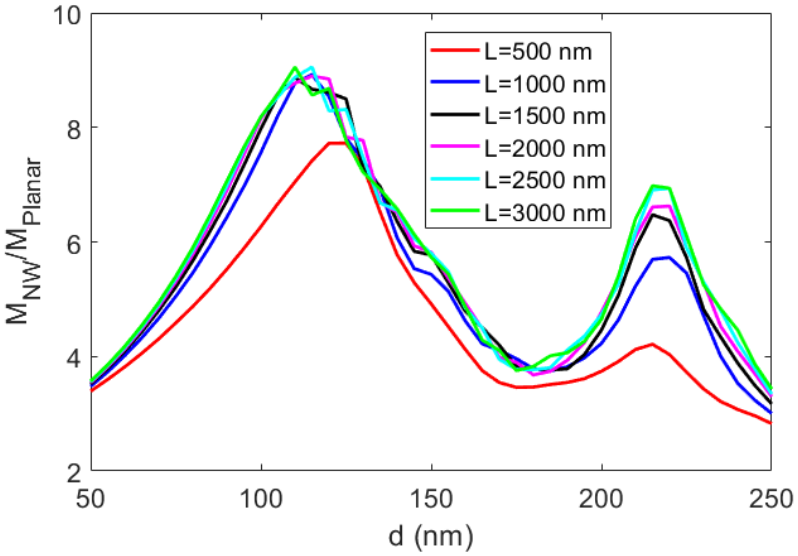

Figure S6. $M_{\mathrm{NW}}/\mathrm{M}_{\mathrm{Planar}}$ for varying L at NA = 1, λ = 640 nm, and t_{oxide} = 10 nm. The simulations are performed with a step of 5 nm in d.

Wavelength dependence of the enhancement

At λ = 640 nm, n = 3.31 for GaP and 1.77 for Al_2O_3. At λ = 550 nm, n = 3.45 + i0.001 for GaP and 1.77 for Al_2O_3. At λ = 450 nm, n = 3.87 + i0.078 for GaP and 1.78 for Al_2O_3. The imaginary part of n, which gives to absorption, is negligible in GaP still at λ = 550 nm (the absorption length in bulk GaP, given by $(4\pi \mathrm{Im}(n)/\lambda)^{-1}$, is 40 μm). However, at λ = 450 nm, the absorption length has decreased to 460 nm.

In Figure S7, we show the bleaching rate modification for these three excitation wavelengths. The peak that shows up at d = 115 nm for λ = 550 nm has shifted to d = 95 nm for λ = 550 nm and d = 70 nm for λ = 450 nm. This shift corresponds extremely well to the shifting to $d' = d^*[\lambda'/\lambda]^*[\mathrm{Re}(n(\lambda))/\mathrm{Re}(n(\lambda'))]$ observed for diameter-dominated resonances in nanowires [34], which predicts a shift to d = 95 nm and 69 nm (this equation originates from the assumption that for a given resonance, the optical path length around the circumference of the nanowire, which is proportional to $d^*\mathrm{Re}(n(\lambda))/\lambda$, should be kept constant to stay at the resonance when d and/or λ is varied).

In the simulations, the second peak at d = 220 nm at λ = 640 nm shifts to d = 180 at λ = 640 nm and d = 130 nm at λ = 450 nm. The prediction from the change in λ and Re(n) is a shift to d = 181 and 132 nm, respectively, in excellent agreement with the peak positions in the simulations. Notice that for λ = 450 nm, an additional higher order resonance shows up at d = 180 nm.

Based on these results, we see that by tuning λ, we can in a predictable manner tune at which d the peak enhancement occurs (if we know at which d the peak occurs for one given λ, or at which λ the peak occurs for one given d).

Also, we see that for λ = 450 nm, the absorption in the GaP, through the non-negligible Im($\underline{n}$), causes a noticeable decrease in $M_{\mathrm{NW}}/\mathrm{M}_{\mathrm{Planar}}$ (black line) as compared to the results from simulation where Im(n) = 0 was set for GaP (magenta line).

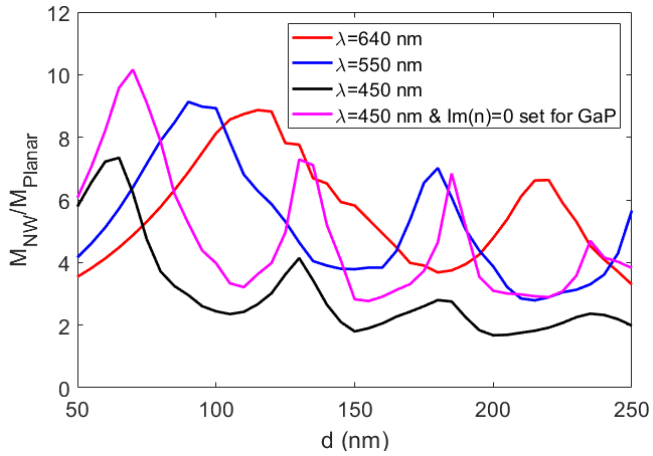

Figure S7. $M_{\mathrm{NW}}/M_{\mathrm{Planar}}$ for $L = 2000$ nm at NA = 1, and t_{oxide} = 10 nm. The simulations are performed with a step of 5 nm in d.

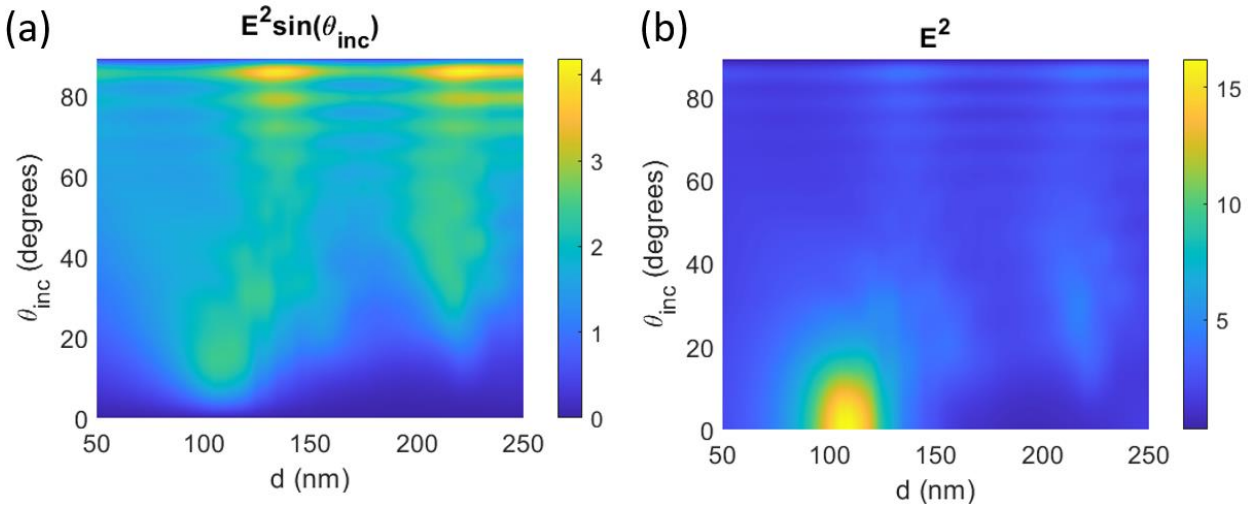

Figure S8. Enhancement for varying incidence angle for $L = 2000$ nm at λ = 640 nm, and t_{oxide} = 10 nm. The simulations are performed with a step of 5 nm in d. Here, we show in (a) the quantity

$$\frac{dM_{NW,\theta_{\mathrm{inc}}}(\theta_{\mathrm{inc}})}{d\theta_{\mathrm{inc}}} = \frac{\int_{z=t_{\mathrm{oxide}}}^{z=t_{\mathrm{oxide}}+L}\int_{r=d/2+t_{\mathrm{oxide}}}^{r=d/2+t_{\mathrm{oxide}}+\Delta_{\mathrm{Fluor}}}\sum_{pol=s,p}\frac{1}{2}\int_0^{2\pi}|\mathbf{E}(\mathbf{r},\lambda,\theta_{\mathrm{inc}},\phi_{\mathrm{inc}},pol)|^2\sin(\theta_{\mathrm{inc}})d\phi_{\mathrm{inc}}rdrdz}{\frac{L\left[(d/2+t_{\mathrm{oxide}}+\Delta_{\mathrm{Fluor}})^2-(d/2+t_{\mathrm{oxide}})^2\right]}{2}} =$$

$$\sin(\theta_{\mathrm{inc}})\frac{\int_{z=t_{\mathrm{oxide}}}^{z=t_{\mathrm{oxide}}+L}\int_{r=d/2+t_{\mathrm{oxide}}}^{r=d/2+t_{\mathrm{oxide}}+\Delta_{\mathrm{Fluor}}}\sum_{pol=s,p}\frac{1}{2}\int_0^{2\pi}|\mathbf{E}(\mathbf{r},\lambda,\theta_{\mathrm{inc}},\phi_{\mathrm{inc}},pol)|^2 d\phi_{\mathrm{inc}}rdrdz}{L[(d/2+t_{\mathrm{oxide}}+\Delta_{\mathrm{Fluor}})^2-(d/2+t_{\mathrm{oxide}})^2]/2}.$$ Note that $M_{NW} =$

$\int_0^{\theta_{NA}} \left(dM_{NW,\theta_{inc}} / d\theta_{inc} \right) d\theta_{inc}$. In (b), we show $\frac{\int_{z=t_{oxide}}^{z=t_{oxide}+L} \int_{r=d/2+t_{oxide}}^{r=d/2+t_{oxide}+\Delta_{Fluor}} \sum_{pol=s,p} \frac{1}{2} \int_0^{2\pi} |\mathbf{E}(\mathbf{r},\lambda,\theta_{inc},\phi_{inc},pol)|^2 d\phi_{inc} r dr dz}{L[(d/2+t_{oxide}+\Delta_{Fluor})^2-(d/2+t_{oxide})^2]/2}$ that corresponds to the electric field enhancement for varying incidence angle.

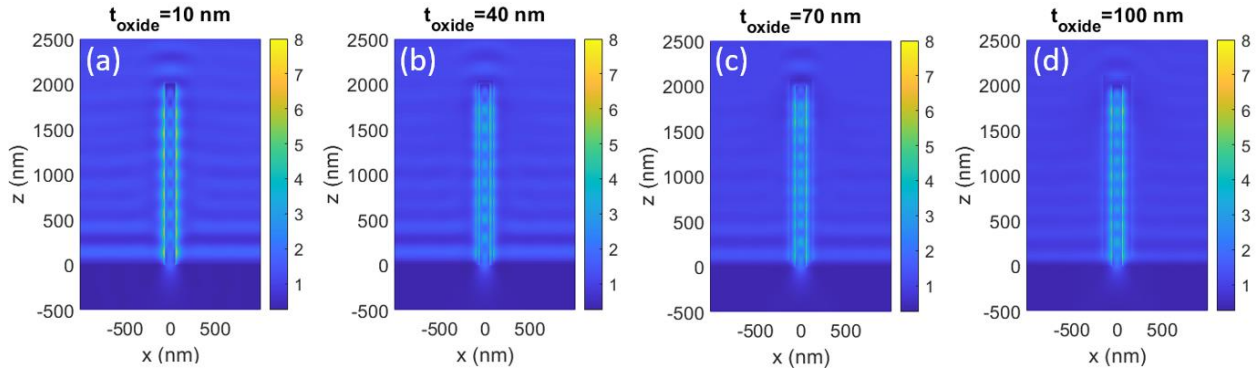

Figure S9. Same as Figure 1(b) for t_{oxide} = 10 nm in (a), but here additionally also for (b) t_{oxide} = 40 nm, (c) t_{oxide} = 70 nm, (d) t_{oxide} = 100 nm.

AUTHOR INFORMATION

Corresponding Author

Heiner Linke heiner.linke@ftf.lth.se

Author Contributions

The manuscript was written through contributions of all authors. All authors have given approval to the final version of the manuscript.

Funding Sources

Swedish Research Council (project numbers 2015-03824, 2019-02435, 2020-04226).

European Union's Horizon 2020 research and innovation programme under grant agreement No 732482 (Bio4Comp).

ACKNOWLEDGMENT

NWs were grown and characterized in Lund Nano Lab (LNL), we are grateful to Peter Blomqvist and Sungyoun Ju for technical support. We are also grateful to Dr. Gerda Rentschler for her help during photobleaching experiments. Procedures for the experiments and image analysis were based on those developed by Dr. Damiano Verardo. We acknowledge the computational resources provided by the Aalto Science-IT project. We also acknowledge Profs. Magnus Borgström, Jonas Tegenfeldt, Martin Magnusson, the members of their groups and the other members of our groups for useful discussions and help.

ABBREVIATIONS

ALD, atomic layer deposition; NW, nanowire; NA, numerical aperture; SEM, scanning electron microscopy.

REFERENCES

(1) Dorfman, A.; Kumar, N.; Hahm, J. Highly Sensitive Biomolecular Fluorescence Detection Using Nanoscale ZnO Platforms. *J. Phys. Chem. Solids* **2005**, *23* (7), 4890–4895. https://doi.org/10.1021/la053270.

(2) Dorfman, A.; Kumar, N.; Hahm, J. I. Highly Sensitive Biomolecular Fluorescence Detection Using Nanoscale ZnO Platforms. *Langmuir* **2006**, *22* (11), 4890–4895. https://doi.org/10.1021/la053270+.

(3) Hu, W.; Liu, Y.; Zhu, Z.; Yang, H.; Li, C. M. Randomly Oriented ZnO Nanorods as Advanced Substrate for High-Performance Protein Microarrays. *ACS Appl. Mater. Interfaces* **2010**, *2* (6), 1569–1572. https://doi.org/10.1021/am100314w.

(4) Hu, W.; Liu, Y.; Yang, H.; Zhou, X.; Li, C. M. ZnO Nanorods-Enhanced Fluorescence for Sensitive Microarray Detection of Cancers in Serum without Additional Reporter-Amplification. *Biosens. Bioelectron.* **2011**, *26* (8), 3683–3687. https://doi.org/10.1016/j.bios.2011.01.045.

(5) Du, B.; Tang, C.; Zhao, D.; Zhang, H.; Yu, D.; Yu, M.; Balram, K. C.; Gersen, H.; Yang, B.; Cao, W.; Gu, C.; Besenbacher, F.; Li, J.; Sun, Y. Diameter-Optimized High-Order Waveguide Nanorods for Fluorescence Enhancement Applied in Ultrasensitive Bioassays. *Nanoscale* **2019**, *11* (30), 14322–14329. https://doi.org/10.1039/c9nr02330e.

(6) Wang, T.; Centeno, A.; Darvill, D.; Pang, J. S.; Ryan, M. P.; Xie, F. Tuneable Fluorescence Enhancement of Nanostructured ZnO Arrays with Controlled Morphology. *Phys. Chem. Chem. Phys.* **2018**, *20* (21), 14828–14834. https://doi.org/10.1039/c8cp01493k.

(7) Ten Siethoff, L.; Lard, M.; Generosi, J.; Andersson, H. S.; Linke, H.; Månsson, A. Molecular Motor Propelled Filaments Reveal Light-Guiding in Nanowire Arrays for Enhanced Biosensing. *Nano Lett.* **2014**, *14* (2), 737–742. https://doi.org/10.1021/nl404032k.

(8) Verardo, D.; Liljedahl, L.; Richter, C.; Agnarsson, B.; Axelsson, U.; Prinz, C. N.; Höök, F.; Borrebaeck, C. A. K.; Linke, H. Fluorescence Signal Enhancement in Antibody Microarrays Using Lightguiding Nanowires. *Nanomaterials* **2021**, *11* (1), 227. https://doi.org/10.3390/nano11010227.

(9) Zhao, X.; Alizadeh, M. H.; Reinhard, B. M. Harnessing Leaky Modes for Fluorescence Enhancement in Gold-Tipped Silicon Nanowires. *J. Phys. Chem. C* **2016**, *120* (37), 20555–20562. https://doi.org/10.1021/acs.jpcc.5b11702.

(10) Kandziolka, M.; Charlton, J. J.; Kravchenko, I. I.; Bradshaw, J. A.; Merkulov, I. A.; Sepaniak, M. J.; Lavrik, N. V. Silicon Nanopillars as a Platform for Enhanced Fluorescence Analysis. *Anal. Chem.* **2013**, *85* (19), 9031–9038. https://doi.org/10.1021/ac401500y.

(11) Frederiksen, R. S.; Alarcon-Llado, E.; Madsen, M. H.; Rostgaard, K. R.; Krogstrup, P.; Vosch, T.; Nygå, J.; Fontcuberta I Morral, A.; Martinez, K. L. Modulation of Fluorescence Signals from Biomolecules along Nanowires Due to Interaction of Light with Oriented Nanostructures. **2021**, *10*, 45. https://doi.org/10.1021/nl503344y.

(12) Verardo, D.; Lindberg, F. W.; Anttu, N.; Niman, C. S.; Lard, M.; Dabkowska, A. P.; Nylander, T.; Månsson, A.; Prinz, C. N.; Linke, H. Nanowires for Biosensing: Lightguiding of Fluorescence as a Function of Diameter and Wavelength. *Nano Lett.* **2018**, *18* (8), 4796–4802. https://doi.org/10.1021/acs.nanolett.8b01360.

(13) Truong, J.; Singh, M.; Hansen, M.; Hahm, J. I. Polarization-Resolved Mechanistic Investigation of Fluorescence Signal Intensification on Zinc Oxide Nanorod Ends. *Nanoscale* **2017**, *9* (24), 8164–8175. https://doi.org/10.1039/c7nr02201h.

(14) Singh, M.; Song, S.; Hahm, J. I. Unique Temporal and Spatial Biomolecular Emission Profile on Individual Zinc Oxide Nanorods. *Nanoscale* **2014**, *6* (1), 308–315. https://doi.org/10.1039/c3nr05031a.

(15) Lard, M.; Linke, H.; Prinz, C. N. Biosensing Using Arrays of Vertical Semiconductor Nanowires: Mechanosensing and Biomarker Detection. *Nanotechnology* **2019**, *30* (21). https://doi.org/10.1088/1361-6528/ab0326.

(16) Guo, L.; Shi, Y.; Liu, X.; Han, Z.; Zhao, Z.; Chen, Y.; Xie, W.; Li, X. Enhanced Fluorescence Detection of Proteins Using ZnO Nanowires Integrated inside Microfluidic Chips. *Biosens. Bioelectron.* **2018**, *99*, 368–374. https://doi.org/10.1016/j.bios.2017.08.003.

(17) Shrivastava, S.; Triet, N. M.; Son, Y. M.; Lee, W. Il; Lee, N. E. Seesawed Fluorescence Nano-Aptasensor Based on Highly Vertical ZnO Nanorods and Three-Dimensional Quantitative Fluorescence Imaging for Enhanced Detection Accuracy of ATP. *Biosens. Bioelectron.* **2017**, *90*, 450–458. https://doi.org/10.1016/j.bios.2016.09.089.

(18) Verardo, D.; Agnarsson, B.; Zhdanov, V. P.; Höök, F.; Linke, H. Single-Molecule Detection with Lightguiding Nanowires: Determination of Protein Concentration and Diffusivity in Supported Lipid Bilayers. *Nano Lett.* **2019**, *19* (9), 6182–6191. https://doi.org/10.1021/acs.nanolett.9b02226.

(19) Seo, K.; Wober, M.; Steinvurzel, P.; Schonbrun, E.; Dan, Y.; Ellenbogen, T.; Crozier, K. B. Multicolored Vertical Silicon Nanowires. *Nano Lett* **2011**, *11*, 1851–1856. https://doi.org/10.1021/nl200201b.

(20) Anttu, N. Geometrical Optics, Electrostatics, and Nanophotonic Resonances in Absorbing Nanowire Arrays. *Opt. Lett.* **2013**, *38* (5), 730. https://doi.org/10.1364/ol.38.000730.

(21) Gu, Z.; Song, Q.; Xiao, S. Nanowire Waveguides and Lasers: Advances and Opportunities in Photonic Circuits. *Frontiers in Chemistry*. Frontiers Media S.A. January 8, 2021, p 613504. https://doi.org/10.3389/fchem.2020.613504.

(22) Anttu, N.; Mäntynen, H.; Sorokina, A.; Kivisaari, P.; Sadi, T.; Lipsanen, H. Geometry Tailoring of Emission from Semiconductor Nanowires and Nanocones. *Photonics* **2020**, *7* (2). https://doi.org/10.3390/PHOTONICS7020023.

(23) Sinha, G.; Depero, L. E.; Alessandri, I. Recyclable SERS Substrates Based on Au-Coated ZnO Nanorods. *ACS Appl. Mater. Interfaces* **2011**, *3* (7), 2557–2563. https://doi.org/10.1021/am200396n.

(24) Fularz, A.; Almohammed, S.; Rice, J. H. Oxygen Incorporation-Induced SERS Enhancement in Silver Nanoparticle-Decorated ZnO Nanowires. *ACS Appl. Nano Mater.* **2020**, *3* (2), 1666–1673. https://doi.org/10.1021/acsanm.9b02395.

(25) Han, X. X.; Ji, W.; Zhao, B.; Ozaki, Y. Semiconductor-Enhanced Raman Scattering: Active Nanomaterials and Applications. *Nanoscale*. Royal Society of Chemistry April 21, 2017, pp 4847–4861. https://doi.org/10.1039/c6nr08693d.

(26) Aspnes, D. E.; Studna, A. A. *Dielectric Functions and Optical Parameters of Si, Ge, GaP, GaAs, GaSb, InP, InAs, and InSb from 1.5 to 6.0 EV*; 1983; Vol. 27.

(27) Song, L.; Hennink, E. J.; Young, I. T.; Tanke, H. J. Photobleaching Kinetics of Fluorescein in Quantitative Fluorescence Microscopy. *Biophys. J.* **1995**, *68* (6), 2588–2600. https://doi.org/10.1016/S0006-3495(95)80442-X.

(28) Eggeling, C.; Widengren, J.; Rigler, R.; Seidel, C. A. M. M. *Photobleaching of Fluorescent Dyes under Conditions Used for Single-Molecule Detection: Evidence of Two-Step Photolysis*; 1998; Vol. 70, pp 2651–2659. https://doi.org/10.1021/ac980027p.

(29) Dodge, M. J. "Refractive Index." In *Handbook of Laser Science and Technology, Volume IV, Optical Materials: Part 2*; Weber, M. J., Ed.; CRC Press: Boca Raton, 1986; p 30. https://doi.org/10.1201/9781003067955.

(30) Schindelin, J.; Arganda-Carreras, I.; Frise, E.; Kaynig, V.; Longair, M.; Pietzsch, T.; Preibisch, S.; Rueden, C.; Saalfeld, S.; Schmid, B.; Tinevez, J. Y.; White, D. J.; Hartenstein, V.; Eliceiri, K.; Tomancak, P.; Cardona, A. Fiji: An Open-Source Platform for Biological-Image Analysis. *Nature Methods*. Nat Methods July 2012, pp 676–682. https://doi.org/10.1038/nmeth.2019.

(31) Huang, L. K.; Wang, M. J. J. Image Thresholding by Minimizing the Measures of Fuzziness. *Pattern Recognit.* **1995**, *28* (1), 41–51. https://doi.org/10.1016/0031-3203(94)E0043-K.

(32) Otsu, N. A Threshold Selection Method from Gray-Level Histograms. *IEEE Trans Syst Man Cybern* **1979**, *9* (1), 62–66. https://doi.org/10.1109/tsmc.1979.4310076.

(33) Benson, D. M.; Bryan, J.; Plant, A. L.; Gotto, A. M.; Smith, L. C. Digital Imaging Fluorescence Microscopy: Spatial Heterogeneity of Photobleaching Rate Constants in Individual Cells. *J. Cell Biol.* **1985**, *100* (4), 1309–1323. https://doi.org/10.1083/jcb.100.4.1309.

(34) Anttu, N.; Xu, H. Q. Efficient Light Management in Vertical Nanowire Arrays for Photovoltaics. *Opt. Express* **2013**, *21* (S3), A558. https://doi.org/10.1364/oe.21.00a558.